

Failure Behavior of F Shape Non-Persistent Joint under Experimental and Numerical Uniaxial Compression Test

vahab sarfarazi (✉ vahab.sarfarazi@gmail.com)

Hamedan University of Technology

kaveh asgari

Shahid Bahonar University of Kerman

meisam zarei

Hamedan University of Technology

Research

Keywords: PFC2D, Physical test, F shape non-persistent joint

Posted Date: April 6th, 2021

DOI: <https://doi.org/10.21203/rs.3.rs-389405/v1>

License:  This work is licensed under a Creative Commons Attribution 4.0 International License.

[Read Full License](#)

Failure behavior of F shape non-persistent joint under experimental and numerical uniaxial compression test

^{1*}Vahab Sarfarazi, ²Kaveh Asgari, ³Meisam Zarei

^{1*}Academic member, Department of Mining Engineering, Hamedan University of Technology, Hamedan, Iran

²Research Scholar, Department of Mining Engineering, Shahid Bahonar University of Kerman, Kerman, Iran

³Research Scholar, Department of Mining Engineering, Hamedan University of Technology, Hamedan, Iran

Abstract Experimental and discrete element approaches were used to examine the effects of F shape non-persistent joints on the failure behaviour of concrete under uniaxial compressive test. concrete specimens with dimensions of 200 mm×200 mm×50 mm were provided. Within the specimen, F shape non-persistent joint consisting three joints were provided. The large joint length was 6 cm, and the length of two small joints were 2cm. Vertical distance between two small joints change from 1.5 cm to 4.5 cm with increment of 1.5 cm. In constant joint lengths, the angle of large joint change from 0 to 90 with increments of 30. Totally 12 different models were tested under compression test. The axial load rate on the model was 0.05 mm/min. Concurrent with experimental tests, numerical simulation (Particle flow code in two dimension) were performed on the models containing F shape non-persistent joint. Distance between small joints and joint angles were similar to experimental one. the results indicated that the failure process was mostly governed by both of the Distance between small joints and joint angles. The compressive strengths of the samples were related to the fracture pattern and failure mechanism of the discontinuities. Furthermore it was shown that the compressive behaviour of discontinuities is related to the number of the induced tensile cracks which are increased by increasing the joint angle. In the first There were only a few AE hits in the initial stage of loading, then AE hits rapidly grow before the applied stress reached its peak. Furthermore, a large number of AE hits accompanied every stress drop. Finally, the failure pattern and failure strength are similar in both approaches i.e. the experimental testing and the numerical simulation approaches.

Keywords: PFC2D, Physical test, F shape non-persistent joint

1.Introduction

Because of the discontinuities like joints, fractures, faults, and bedding planes, rocks generally shows anisotropy. By comparing rock mass with intact rocks, it can be understood that these discontinuities can change the state of stress. When these kind of rock masses with fractures are loaded, it is possible for new cracks to develop and change their characteristics of strength and deformation. These new born cracks will spread in the loading direction and may causes to macroscopic failures. The impact of these crack formation and subsequent growth under different loading conditions can persuasively characterized by The fracture mechanics theory. Several investigators tried to examine the rock fracture behavior based on crack initiation stress and their propagation (Griffith 1920; Inglis 2013; Orowan 1949; Hoek 1964; Hoek 1965; Barenblatt 1962; Dugdale 1960; Hillerborg 1976; Cao 2020; Haeri 2019; Hu 2020; Kou 2019; Zhao 2018; Zhao 2018; Zhang 2020; Bagher Shemirani 2021). Griffith 1920, was the first investigator which introduce concept of the Fracture mechanics. Griffith by considering a single elliptical open flaw, propose a fracture initiation criterion for brittle materials. He on the study of Inglis 2013 and based on the local stress state for an elliptical open hole in an infinite plate developed the criteria. Griffith's theory supposes that when the stress at the crack tip exceeds the molecular cohesive strength of

material (Orowan 1949) or the uniaxial tensile strength of the material (Hoek 1964), the existing fracture initiates. Thus, some limitation exists, for instance, Hoek and Bieniawski 1965, indicated that Griffith's fracture criterion is developed for the initiation of crack but it does not provide data of the crack propagation direction. Furthermore, Griffith's criteria are developed only for pure brittle materials where plasticity is ignored. But in practical conditions, zone of fracture progress is in front of the pre-existing flaw tip where the plastic deformation happens (Barenblatt 1962). Barenblatt 1962 and Dugdale 1960, Hillerborg 1976 proposed a new model known as cohesive zone model (CZM) based on analytical models. This model considers the plasticity in linear elastic fracture mechanics (LEFM). Some investigators have performed experimental examinations on the growth of cracks in rock or rock like materials under the compressive loads (Bobet 1998; Sagong 2002; Bobet 1998; Wong 2009; Park 2009; Wong 2009; Park 2010; Lin 2020; Lin 2020; Miao 2018; Qian 2020; Wu 2019; Zhou 2018; Zhou 2020; Cheng 2019; Zhang 2018; Zhou 2019; Zhou 2018). Bobet and Einstein 1998 a and 1998b and Sagong and Bobet 2002, have performed an investigation on gypsum, a rock like material for recording pattern of crack and their spread for open and narrow flaws. In addition, Wong and Einstein 2009a and 2009b provide a better comprehension from crack propagation types, they

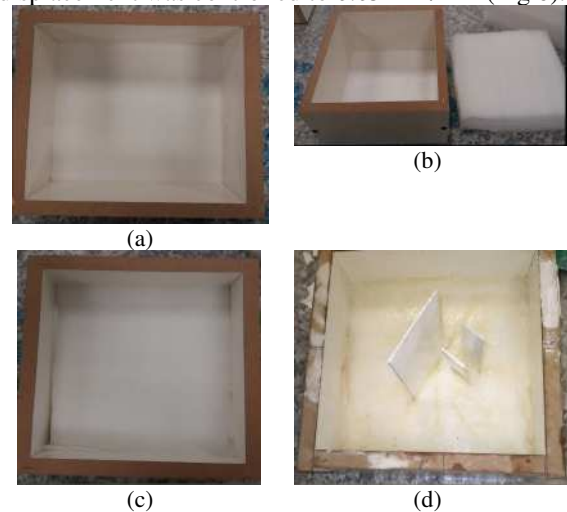
used the high speed camera in their study and provides a good visualization. Although, in these previous studies the stress of crack initiation was covered, the influence of friction behavior was ignored in their experimental study Park 2009 and Park 2010. Furthermore, the process of fracturing was proved to be identical for both open and closed flaws, the influence of stresses proved to be varying. Simultaneously with improvement of computational techniques, the researches on the stresses of crack and its spread are extended into numerical approaches (Reyes 1991; Xu 2011; Gonc 2013; Xie 2016; Yang 2020; Yang 2018; Zhang 2019; Zhou 2019). Several numerical approaches exist such as finite element method (FEM) (Hillerborg 1976; Reyes 1991; Xu 2011; Gonc 2013; Xie 2016), discrete element approach (Lee 2011), hybrid finite-discrete element approaches (Lisjak 2014; Mahabadi 2012) and displacement discontinuity approach (Vasarhelyi 2000) to investigate the crack initiation and spread by various criteria based on fracture mechanics. For modelling the material which has a pre-existing flaw in a continuum medium FEM is known as one of best adopted methods. Hillerborg 1976, tried to consider CZM into FEM for concrete materials. Later Reyes and Einstein 1991, and Gonc 2013, by considering three various fracture criterion known as principal stress, principal strain and energy criterion adopted it on FEM for rock and rock like materials. Although there is good correlation with experimental studies, the numerical model does not account for frictional impact between the flaws. Most of these investigations are on the rock with open flaws, under compressive loading where the flaw remains open throughout the loading history. Domain rock may show both open flaws and closed (narrow) flaws, which the second one closes under the loading and causes to surface friction between the flaws (Xie 2016). Because of this behavior, crack initiation and peak stresses of the material can be varied. The studies on the crack with narrow flaw under compressive loading showed that the crack initiation stress compared to open flaw is higher (Park 2009; Park 2010; Reyes 1991). Steif 1984(Steif 1984; Horri 1985; Ashby 1986; Baud 1996), Horii and Nemat-Nasser 1985, Ashby and Hallam 1986 and Baud et al. 1996, have accounted the effect of frictional behavior across the flaw surface into analytical examinations. To comprehend the influence of crack surface friction Xie et al. 2016; carried out the numerical analyses using extended finite element method based on LEFM. But, only the crack initiation stress has considered in their adopted numerical criteria. The later effect of propagation after initiation of crack and the material threshold strength (peak stress) are not included.

In this study, uniaxial tests for rock like model containing F shape non-persistent joints were carried out using experimental test and numerical simulations (PFC). Two parameters were changed i.e. Joint angle and distance between two small joints.

2. Uniaxial compression test for rock-like specimens with F shape joint

In these experiments Rock-like materials were used to simulating fractured rock masses. The materials were blended well and a weight ratio of 2 to 1 cement to water was prepared. The specimen size (length * width * height) was 20 cm * 20 cm * 10 cm. To create F shape non-persistent joint, three thin metal plate is pre-inserting into the material and removing it after initial hardening of specimen (Fig. 1). To remove accidental error and increase the scientifically of the experiment, three similar prefabricated crack test blocks were provided for each group. Linear non-persistent cracks were formed in the model.

The large joint length was 6 cm, and the length of two small joints were 2cm (Fig 2). Vertical distance between two small joints (a in Fig. 2) changes from 1.5 cm to 4.5 cm with increment of 1.5 cm. In constant joint lengths, the angle of large joint (α in Fig. 2) change from 0 to 90 with increments of 30. Totally 12 specimens were prepared. The samples were placed in a cool and ventilated condition for 28 days (Figs 3-5). The electrohydraulic universal testing machine was used to performing the uniaxial compression test for the non-persistent joints. The experimental system includes the test bed, loading control system and data acquisition system. The specimens were placed in the center of the base and maintained the horizontal contact with the base. in the experiment, the rate of loading displacement was controlled to 0.05 mm/min (Fig 6).



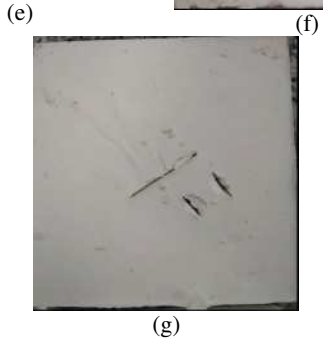


Fig 1. a) the frame with dimensions of 200mm× 200mm × 100mm, b and c) a unique plastic fiber with dimension of 200mm × 200 mm × 50 mm was put into the frame, d) the shim within the plastic fiber, e) slurry within the box, f) the aluminum sheet was taken out from the mold, g) the physical sample.

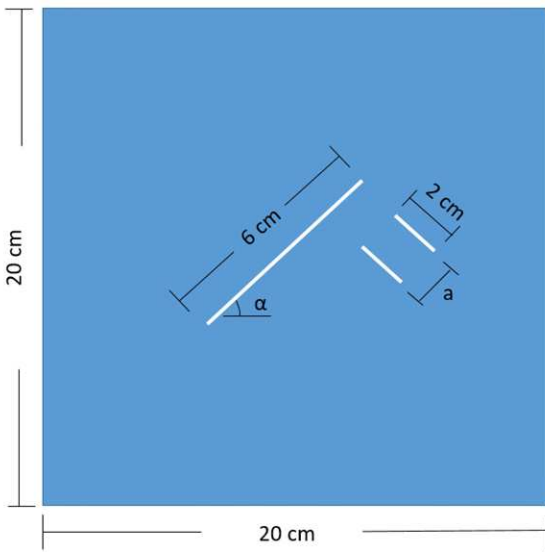


Fig 2. F shape non persistent joints

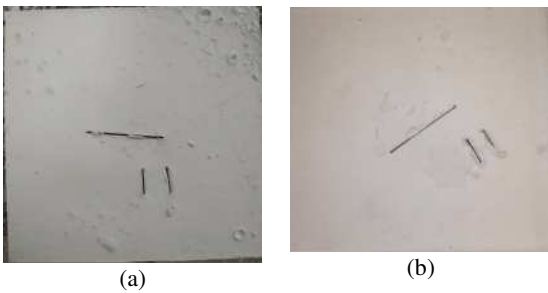


Fig 3. F shape non persistent joints with large joint angle of; a) 0, b) 30, c) 60, d) 90; vertical distance between small joint was 1.5cm.

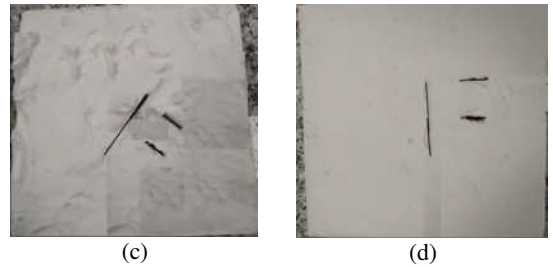


Fig 4. F shape non persistent joints with large joint angle of; a) 0, b) 30, c) 60, d) 90; vertical distance between small joint was 3cm.

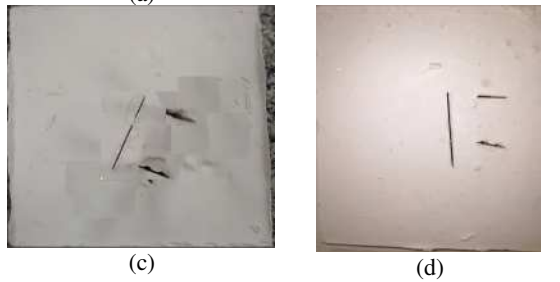
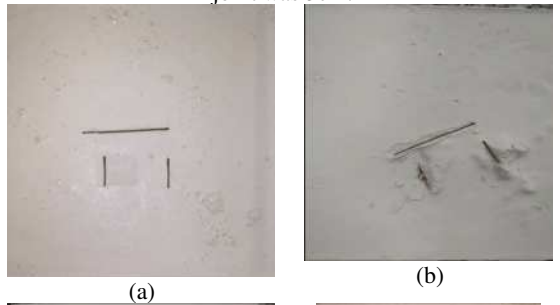


Fig 5. F shape non persistent joints with large joint angle of; a) 0, b) 30, c) 60, d) 90; vertical distance between small joint was 4cm.



Fig 6. Specimen are placed between the plates of the loading machine.

3. Experimentally observed failure patterns

3.1. Failure pattern of experimental specimens

a) Distance between small joints was 1.5 cm

Fig. 7 shows the failure pattern of specimens with large joint angle of 0, 30, 60, and 90. When the angle of large joint was 0 (Fig. 7a), two tensile wing cracks originated from large joint and distributed parallel to loading axis till integrated with boundaries of specimen. One of the vertical small joint was mobilized in failure process. When the angle of large joint was 30 (Fig. 7b), two tensile wing cracks originated from large joint and distributed parallel to loading axis till integrated with boundaries of specimen. The small joints have not any effect in failure process. When the angle of large joint was 60 (Fig. 7c), two tensile wing cracks originated from both of the large joint and small joint and propagated parallel to loading axis till integrated with boundaries of sample. Also, rock bridges were broken by two oriented wing cracks. When the angle of large joint was 90 (Fig. 7d), two tensile wing cracks originated from small joints and propagated parallel to loading axis till integrated with boundaries of specimen. The large joint has not any effect in failure process.

In these configuration, splitting failure was occurred in sample. The Failure surface was smooth without pulverized material. This is representative of tensile crack.

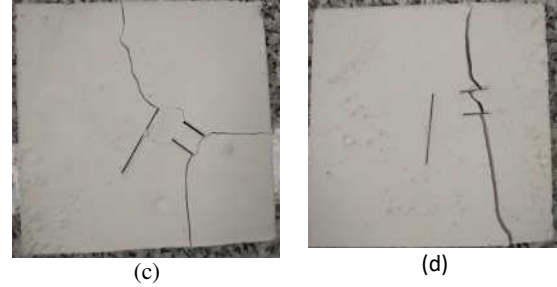
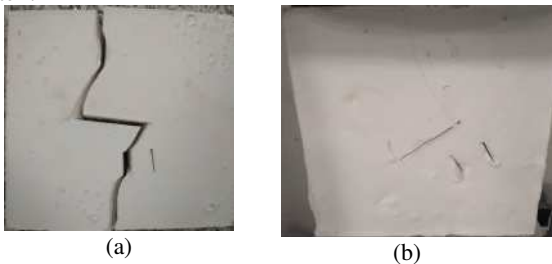


Fig 7. Failure pattern in F shape non persistent joints with large joint angle of; a) 0, b) 30, c) 60, d) 90; vertical distance between small joint was 1.5cm.

b) Distance between small joints was 3 cm

Fig. 8 shows the failure pattern of samples with large joint angle of 0, 30, 60, and 90. When the angle of large joints was 0 (Fig. 8a) and 30 (Fig. 8b), two tensile wing cracks originated from large joint and distributed parallel to loading axis till integrated with boundaries of specimen. One of the vertical small joint was mobilized in failure process. When the angle of large joint was 60 (Fig. 8c), two tensile wing cracks originated from both of the large joint and small joint and spread parallel to loading axis till integrated with boundaries of specimen. Also, rock bridges were broken by two oriented wing cracks. When the angle of large joint was 90 (Fig. 8d), two tensile wing cracks originated from small joints and propagated parallel to loading axis till integrated with boundaries of sample. The large joint has not any effect in failure process. In these configuration, splitting failure was occurred in sample. The Failure surface was smooth without pulverized material. This is representative of tensile crack..

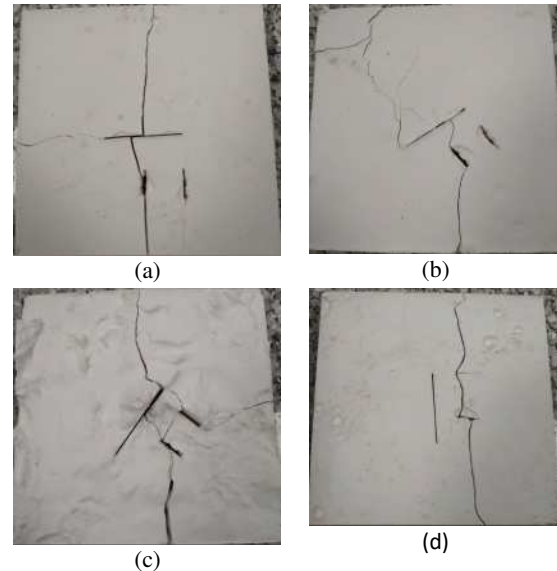


Fig 8. Failure pattern in F shape non persistent joints with large joint angle of; a) 0, b) 30, c) 60, d) 90; vertical distance between small joint was 3cm.

c) Distance between small joints was 4.5 cm

Fig. 9 shows the failure pattern of samples with large joint angle of 0, 30, 60, and 90. When the angle of large joint was 0 (Fig. 9a), two tensile wing cracks originated from large joint and distributed parallel to loading axis till integrated with boundaries of specimen. One of the vertical small joint was mobilized in failure process. When the angle of large joint was 30 (Fig. 9b), two tensile wing cracks originated from large joint and distributed parallel to loading axis till integrated with boundaries of specimen. The small joints have not any effect in failure process. When the angle of large joint was 60 (Fig. 9c), two tensile wing cracks originated from large joint and distributed parallel to loading axis till integrated with boundaries of sample. One of the vertical small joint was mobilized in failure process. When the angle of large joint was 90 (Fig. 9d), two tensile wing cracks originated from small joints and propagated parallel to loading axis till integrated with boundaries of specimen. In these configuration, splitting failure was occurred in sample. The Failure surface was smooth without pulverized material. This is representative of tensile crack.

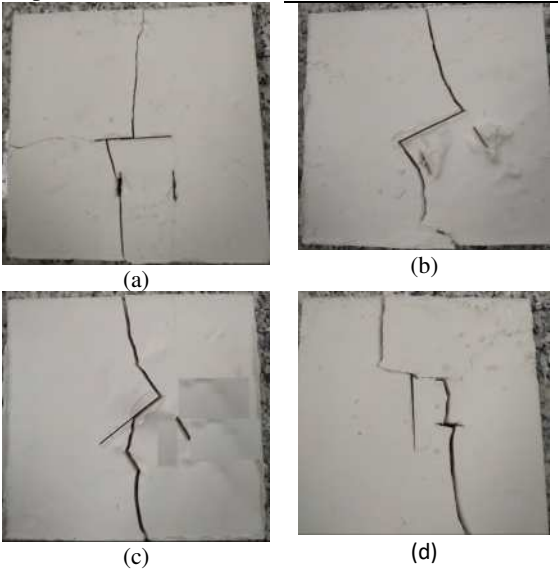


Fig 9. Failure pattern in F shape non persistent joints with large joint angle of; a) 0, b) 30, c) 60, d) 90; vertical distance between small joint was 4.5cm.

3.2. The influence of joint spacing and joint angle on the strength of samples

Fig 10 shows the effect of joint angle on the strength of models. This figure was presented for three joint spacing. The strength of specimen was increased by increasing the joint spacing. The minimum of compressive strength occurs when joint angle was 30.

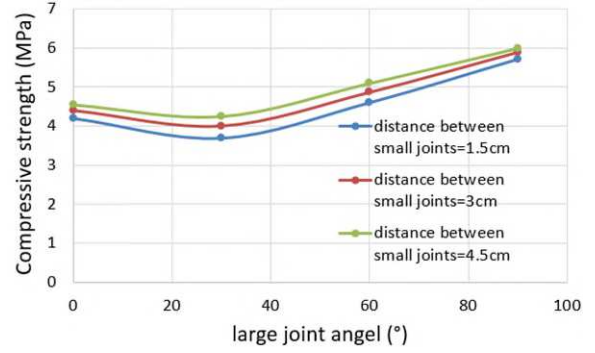


Fig 10 the influence of joint angle on the strength of models.

4 Numerical Model

4.1 Particle Flow Code

Potyondy (2012) proposed the flat-joint (FJ) model by considering the polygonal grain structure of particles. as shown in Figure 11 The FJ contact is depicting as locally flat notional surfaces centered at the contact point and attached rigidly to a piece of particle. each piece has a face which is its notional surface and interacts with the face of contacting piece. Thus, each faced grain is showed as a circular (2D) or spherical (3D) core with skirted faces. These faces are lines (in 2D) or disks (in 3D). The assembly of particles bonded by FJ contacts is called flat-jointed material (FJM). The boundary between faced grains is discretized into elements which elements can be either bonded or unbonded. Then FJ installed at a grain–grain contact and torque and force at each element are set to zero and updated based on the force–displacement law of bond and relative motion of faces. The shear force is updated in an incremental mode while the normal force is updated in a direct mode. As long as the strength doesn't exceed its limit, the behavior of bonded element remains linear elastic. The measurement of The maximum normal and shear stresses of element ($\sigma_{max}^{(e)}, \tau_{max}^{(e)}$) is based on the following:

$$\sigma_{max}^{(e)} = \frac{-\bar{F}_{(e)}^n}{A^{(e)}} \quad (1)$$

$$\tau_{max}^{(e)} = \frac{\bar{F}_{(e)}^s}{A^{(e)}} \quad (2)$$

Where $A^{(e)}$ is the element area and $\bar{F}_{(e)}^n$ and $\bar{F}_{(e)}^s$ are normal and shear forces acting on the element, respectively. A special structure of faced grains is provided the rotational resistance of elements and the torque contributions are negligible. As mentioned above, the FJ elements can be bonded or unbonded. The strength of bonded element is based on the Coulomb criterion with the tension cut-off. When the normal stress is greater than the element tensile strength ($\sigma_{max}^{(e)} > \sigma_b$), element breaks in tension followed

by tensile crack generation and modification of the element state to unbonded. The shear strength of element is specified by the bond cohesion c_b and the local friction angle ϕ_b . When the shear stress is greater than the shear strength of element $[\tau_{max}^{(e)} > \tau_c = c_b - \bar{\sigma} \tan \phi_b]$, the bond breaks in shear and the bond state modified to unbonded with residual frictional strength. The mechanical behavior of unbonded element is linear elastic with frictional slip. The force–displacement law is as follows,

$$\bar{\sigma} = \begin{cases} 0 & \bar{g} \geq 0 \\ -k_n \bar{g} & \bar{g} < 0 \end{cases} \quad (3)$$

$$\bar{\tau} = \begin{cases} -\bar{\sigma} \tan \phi_r & \bar{\sigma} < 0 \\ 0 & \bar{\sigma} = 0 \end{cases} \quad (4)$$

where \bar{g} is the element gap, $\tan \phi_r$ is the friction coefficient of unbonded element and ϕ_r is the residual friction angle. The breakage of each bonded element causes to a partial harm of the FJ contact. When the relative displacement at a FJ contact becomes greater than the FJ diameter, the faces are removed and if these particles come back into contact, the force–displacement relationship is that of the linear contact model (Potyondy, 2012, 2015, 2017; Wu & Xu, 2016).

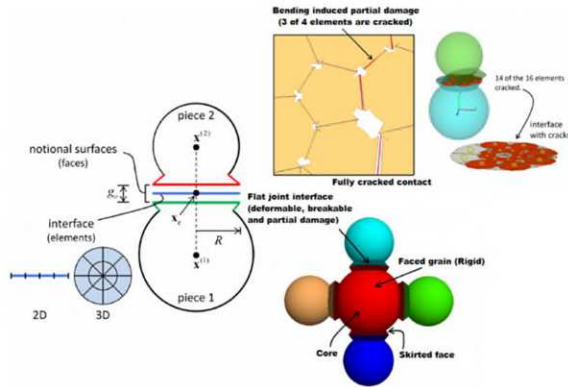


Fig. 11 Flat-joint model (Potyondy, 2015).

4.2 PFC2D Model Preparation and Calibration for Rock-Like Material

In this paper for preparation a test models the standard process of producing a PFC2D assembly were used, this process entirely is described by Potyondy and Cundall 2004. The process consists of particle producing, packing the particles, isotropic stress installation (stress initialization), floating particle (floaters), removing and bond installation. Since the samples were small gravity effect and the gravity-induced stress gradient influence on the macroscopic behavior is negligible. Calibration of particles properties and flat joint model were carried out using Uniaxial compressive strength and Brazilian test (Ghazvinian et al. 2012). Adopting the micro-characteristics are listed in Table 1 and the standard calibration methods (Sarfarazi 2014, Sarfarazi 2016 a, b and c), a calibrated PFC particle assembly was generated. Fig 12 a and b depicts the experimental uniaxial compression test and numerical simulation,

respectively. Fig 12 c and d shows experimental Brazilian test and numerical simulation, respectively. The results showed good correlation between experimental test and numerical simulation. Also, as indicated in Table 2 the obtained specimen characteristics from the numerical models such as elastic modulus, Poisson's ratio, UCS values are nearly similar to the experimental values.

Table 1. Micro characteristics used to introduce the intact rock.

Particle micro properties		Flat-joint micro properties	
Model height (mm)	108	Gap ratio	0.5
Model width (mm)	54	Ec (GPa)	0.3
Kn/ks	1.7	Bonded friction	0.83
density	2500	Tensile strength	0.1
Minimum particle diameter	0.54	Tensile strength standard deviation (MPa)	0.01
Maximum particle diameter	1.08	Cohesion (MPa)	0.5
Ec(GPa)	0.3	Cohesion standard deviation (MPa)	0.05
porosity	0.08	Number of elements	2
		Kn/ks	1.7

Table 2. Comparison of macro-mechanical characteristics between experiments and model

Mechanical characteristics	Experimental results	PFC2D Model results
Elastic modulus, (GPa)	5	5
Poisson's ratio	0.18	0.19
UCS, (MPa)	7.4	7.4
Brazilian tensile strength (MPa)	1	1.05

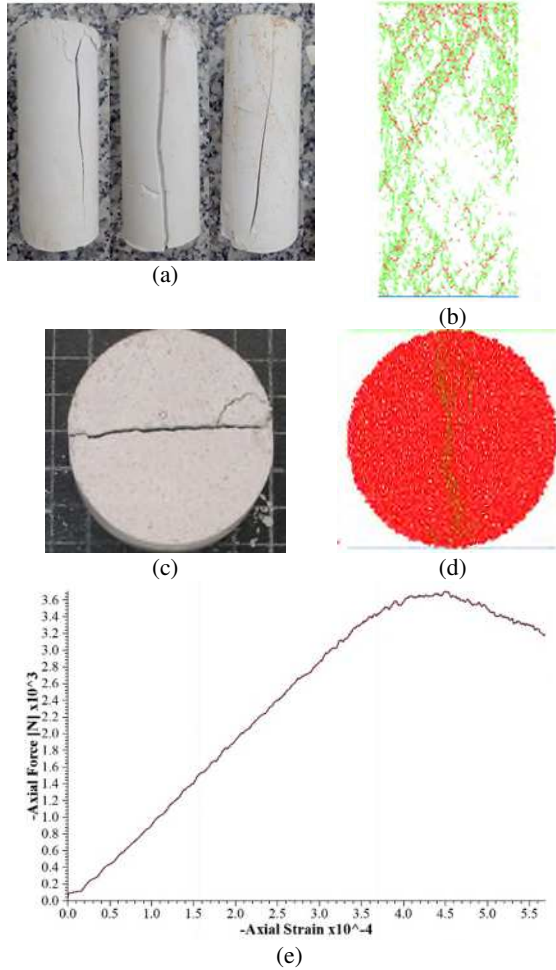


Fig 12. a) Experimental compression test, b) numerical compression test, c) experimental Brazilian test and d) numerical Brazilian test, e) axial force versus axial strain for numerical uniaxial compressive test

4.3. Numerical compressive Tests on the Non-Persistent Open Joint

At first PFC2D was calibrated and then uniaxial tests for jointed rock were numerically simulated by creating a box model in the PFC2D (by using the calibrated micro-parameters) (Figs. 13-15). The dimensions of the PFC sample were 200 mm × 200 mm. The box sample were included a number of 15329 disks with a minimum radius of 0.27 mm.

There are two walls at the upper and lower of the model. The F shape non-persistent joints were created by removing of three bands of particles from the model (Figs. 13-15). The large joint length was 6 cm, and the length of two small joints were 2cm (Fig 13-15). Vertical distance between two small joints changes from 1.5 cm to 4.5 cm with increment of 1.5 cm. In constant joint lengths, the angle of large joint change from 0 to 90 with increments of 30 (Figs. 13-15). Totally 12 specimens were prepared. The crack arrangement and sample number of each sample were showed in Figs. 13-15. It

is important to note that, this joint configuration is identical to experimental one. Upper and lower walls induced uniaxial force on the model. The axial load rate on the model was 0.05 mm/min. The compression force was recorded by registering the reaction forces on the upper wall.

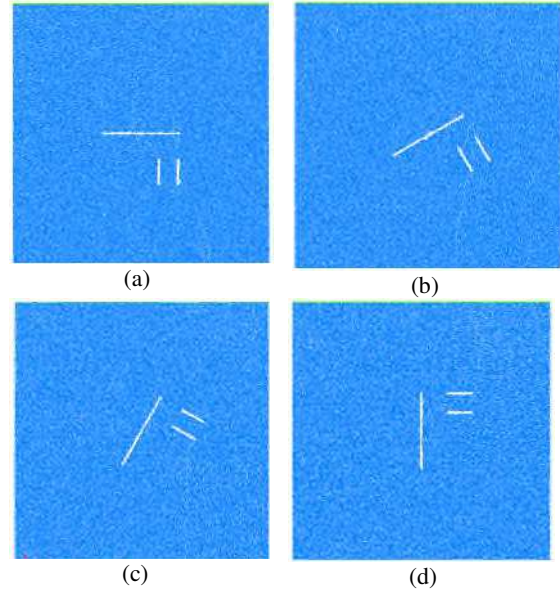


Fig 13. F shape non persistent joints with large joint angle of; a) 0, b) 30, c) 60, d) 90; vertical distance between small joint was 1.5cm.

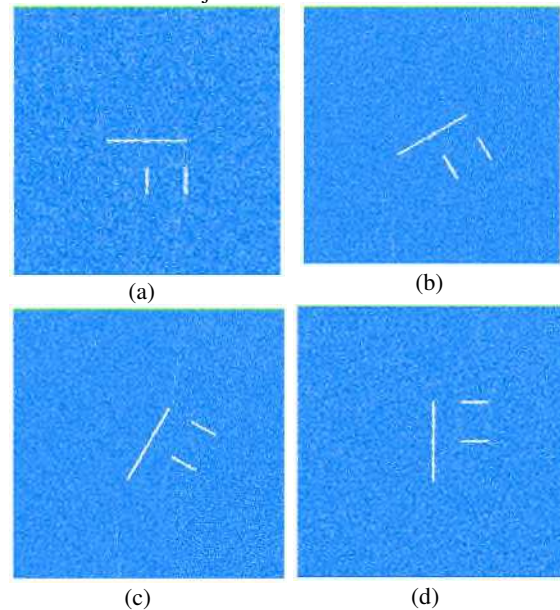


Fig 14. F shape non persistent joints with large joint angle of; a) 0, b) 30, c) 60, d) 90; vertical distance between small joint was 3cm.

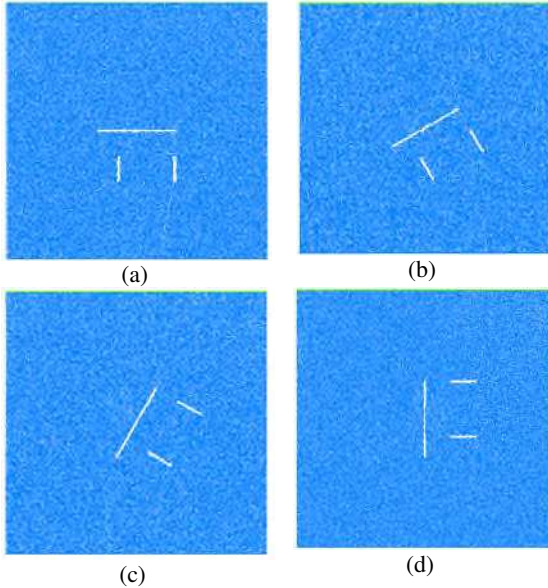


Fig 15. F shape non persistent joints with large joint angle of; a) 0, b) 30, c) 60, d) 90; vertical distance between small joint was 4.5cm.

4.4. mechanism of numerical model Failure

a) Distance between small joints was 1.5 cm

Fig. 16 shows the failure pattern of specimens with large joint angle of 0, 30, 60, and 90. The green line and red line are representative of tensile crack and shear crack, respectively. Fig 17 depicts Ross diagram of crack growth. When the angle of large joint was 0 (Fig. 16a), two tensile wing cracks originated from large joint and distributed parallel to loading axis till integrated with boundaries of specimen. One of the vertical small joint was mobilized in failure process. Rock bridge failure was occurred by two tensile cracks. When the angle of large joint was 30 (Fig. 16b), two tensile wing cracks originated from both of the large joint and small joint and spread parallel to loading axis till integrated with boundaries of sample. Rock bridges were broken by two tensile cracks. When the angle of large joint was 60 (Fig. 16c), two tensile wing cracks originated from both of the large joint and small joint and spread parallel to loading axis till integrated with boundaries of sample. Also, rock bridges were broken by two oriented wing cracks. When the angle of large joint was 90 (Fig. 16d), two tensile wing cracks originated from small joints and spread parallel to loading axis till integrated with boundaries of specimen. The large joint has not any effect in failure process.

From fig 17, the angles of micro cracks varied from 75 to 105 degree. The increasing the joint angle have not any effect on the newborn crack numbers.

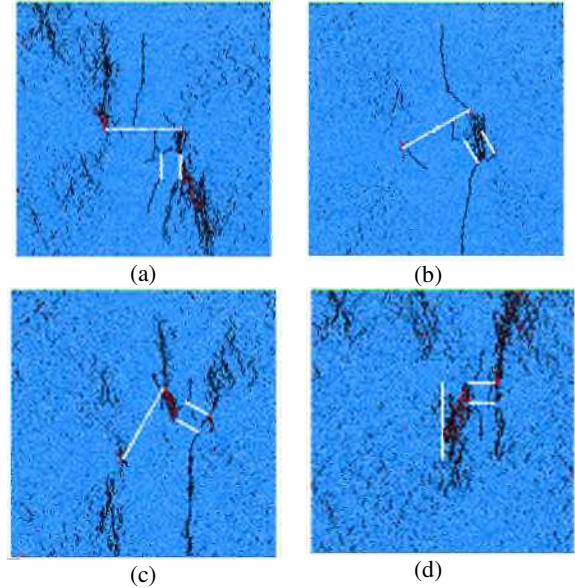
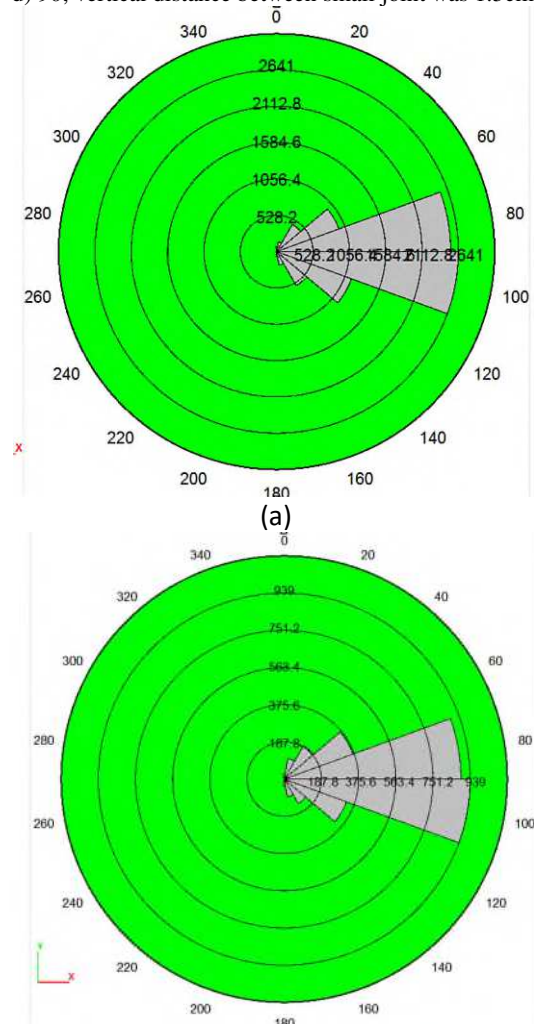


Fig 16. Crack pattern in specimen containing F shape non persistent joints with large joint angle of; a) 0, b) 30, c) 60, d) 90; vertical distance between small joint was 1.5cm.



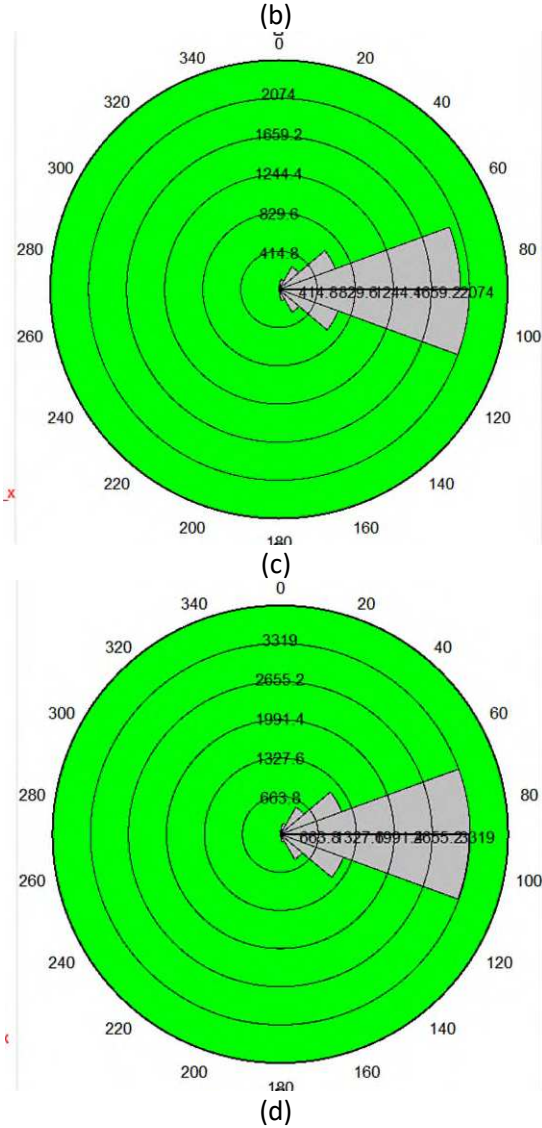


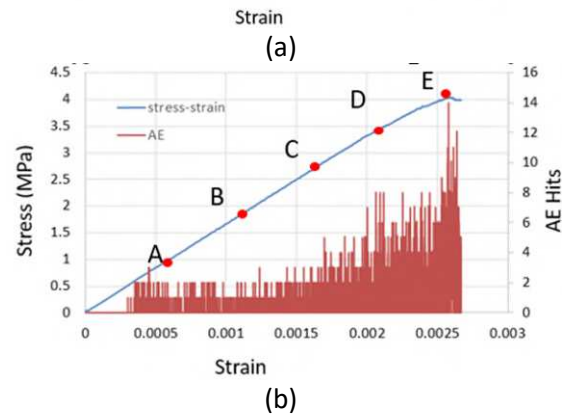
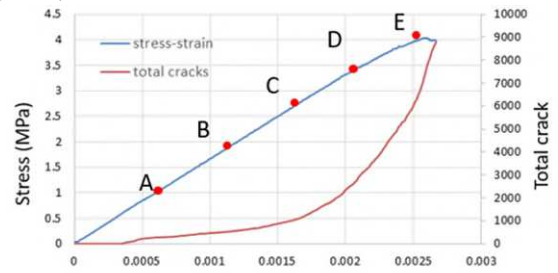
Fig 17 Ross diagram of crack growth for F shape joint with angle of; a) 0, b) 30, c) 60, d) 90.

Fig. 18 a, c, e, g shows the stress-strain curve along with the total crack number for joint angles of 0, 30, 60 and 90. Fig. 18 b, d, f, h shows the stress-strain curve along with AE hits for joint angles of 0, 30, 60 and 90. The reason why we analyze the acoustic emission properties (AE hits) of jointed rock mass in the process of compression is that the engineering rock burst problem is often monitored based on the AE signal in practical engineering. In the PFC model, when the stress between particles is greater than the PB model contact strength, the fracture occurs, that is, an AE hit occurs (Zhang et al, 2018). Therefore, the acoustic emission phenomenon can be simulated by writing fish language to monitor the fracture of the model. Along the stress-strain curve, five points labeled A-E were marked, and the stress at each point

are 20%, 40%, 60%, 80% and 100% of total stress, respectively. The corresponding points were also marked in Fig. 18 b, d, f, h.

The figure showed that with the increase of stress-strain curve until the peak, the AE hits of F shape joints numerical specimens presents three stages. In the first stage, stress less than point A, AE hits is almost zero; this stage is in the elastic stage, and there is no crack in the sample. In the second stage, the stress is about between point A and point C. In this stage, AE hits is in a slowly increasing stage, which is due to the micro cracks in the jointed rock mass continuous expansion. In the third stage, after the C point, the AE hits increase rapidly, because the rock almost enters its bearing limit and the crack propagation speed is very fast. Generally, the maximum value of AE is near the peak value. When the joint length is the same, different joint angle lead to a significant change in the maximum AE hits.

When the small joint angles were 0 and 90, the AE hits was in a slowly increasing trend. When the small joint angle is 30 and 60, the second stage of AE hits does not increase slowly, but there are multiple peaks, which is due to the continuous step expansion of the cracks. This shows that the crack propagation and penetration mechanism and mode of jointed rock specimens are greatly affected by the increase of joint length. Joint angle changes the failure mode of jointed rock sample, and has important effect on the evolution of AE.



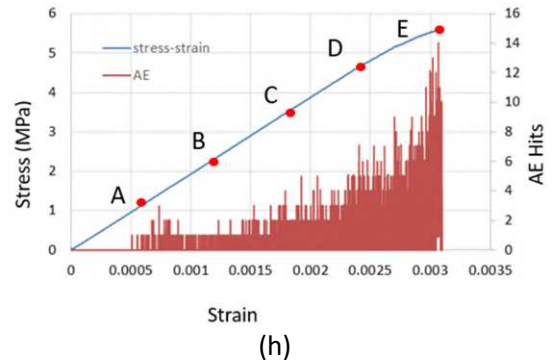
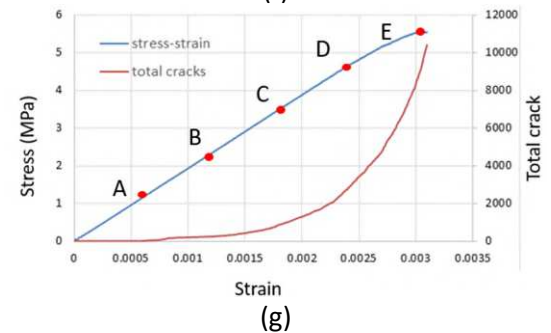
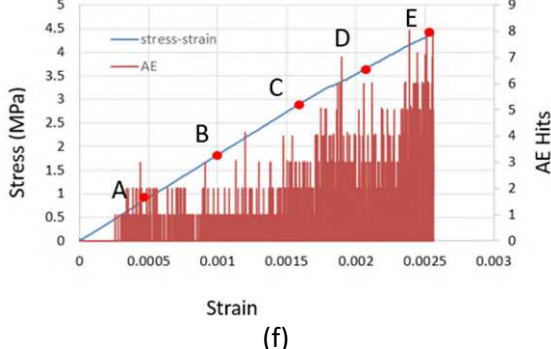
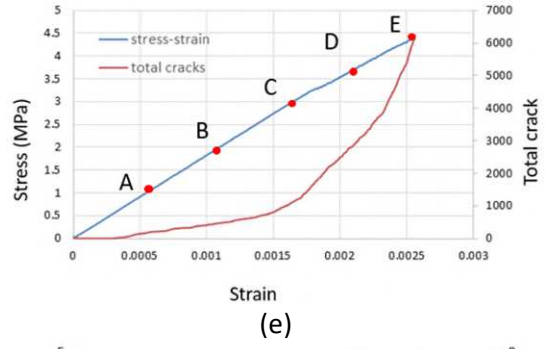
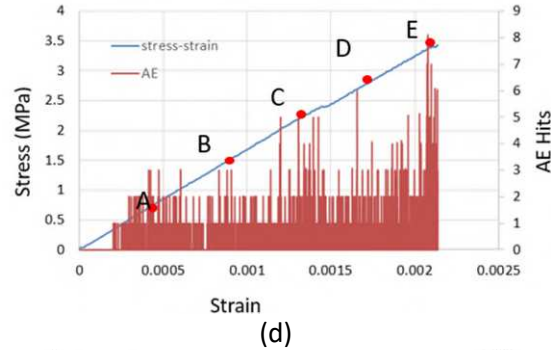
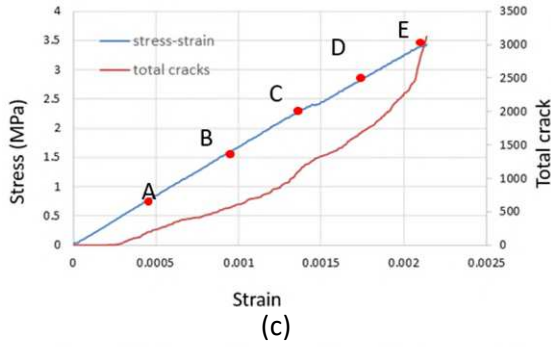


Fig. 18. Stress and AE behavior in the test simulation for joint spacing of 1.5 cm, a) stress-strain curve and cumulative crack number for joint angle of 0, b) the number of AE hits along the strain curve for joint angle of 0, c) stress-strain curve and cumulative crack number for joint angle of 30, d) the number of AE hits along the strain curve for joint angle of 30, e) stress-strain curve and cumulative crack number for joint angle of 60, f) the number of AE hits along the strain curve for joint angle of 60, g) stress-strain curve and cumulative crack number for joint angle of 90, h) the number of AE hits along the strain curve for joint angle of 90.

b) Distance between small joints was 3 cm

Fig. 19 shows the failure pattern of specimens with large joint angle of 0, 30, 60, and 90. The green line and red line are representative of tensile crack and shear crack, respectively. Fig 20 depicts Ross diagram of crack growth. When the angle of large joints was 0 (Fig. 19a) and 30 (Fig. 19b), two tensile wing cracks originated from large joint and spread parallel to loading axis till integrated with boundaries of sample. One of the small joint was mobilized in failure process. When the angle of large joint was 60 (Fig. 19c), two tensile wing cracks originated from both of the large joint and small joint and spread parallel to loading axis till integrated with boundaries of sample. Also, rock bridges were broken by two oriented wing cracks. When the angle of large joint was 90 (Fig. 19d), two tensile wing cracks originated from small joints and spread parallel to loading axis till integrated with boundaries of specimen. The large joint has not any effect in failure process.

From Fig 20, the angles of micro cracks varied from 75 to 105 degree. The increasing of joint angle have not any effect on the newborn crack numbers.

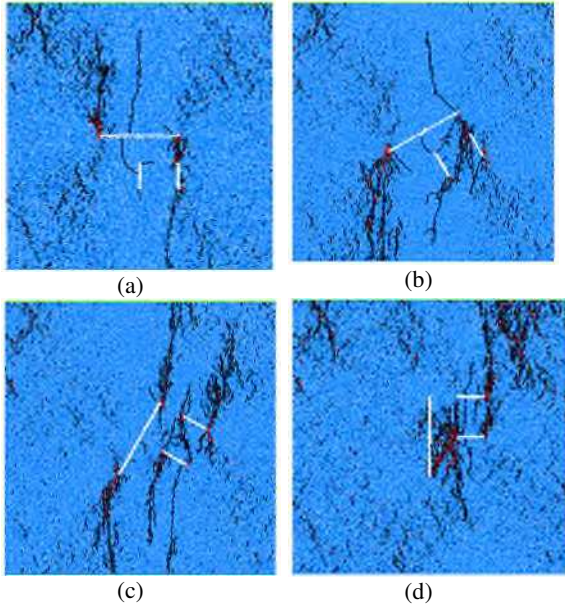


Fig 19. Crack pattern in specimen containing F shape non persistent joints with large joint angle of; a) 0, b) 30, c) 60, d) 90; vertical distance between small joint was 3cm.

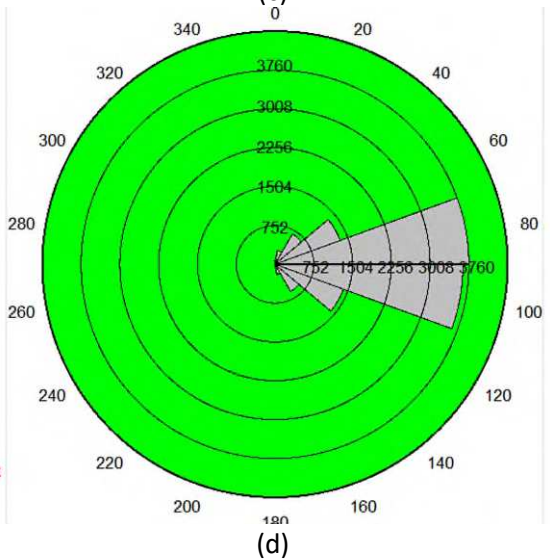
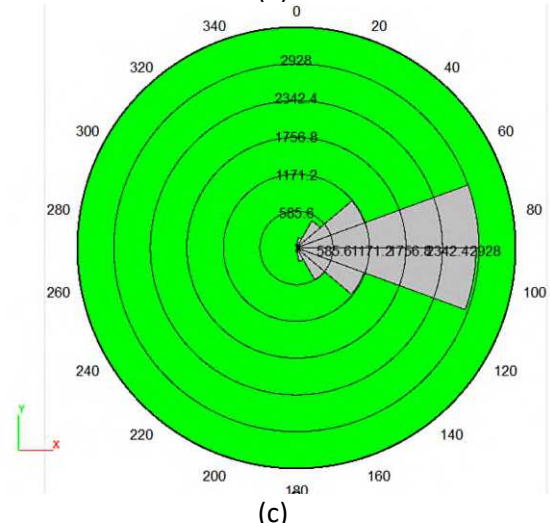
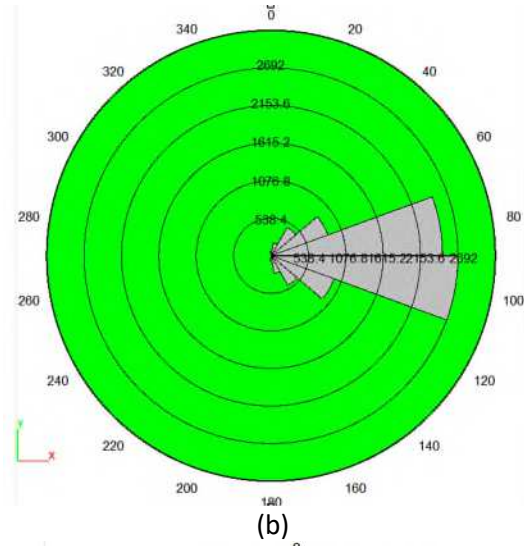
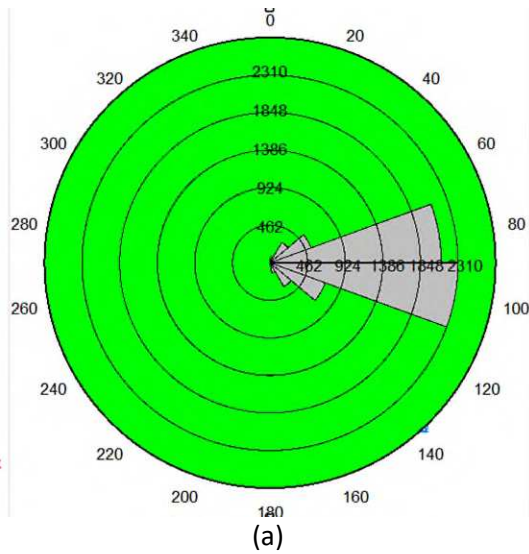
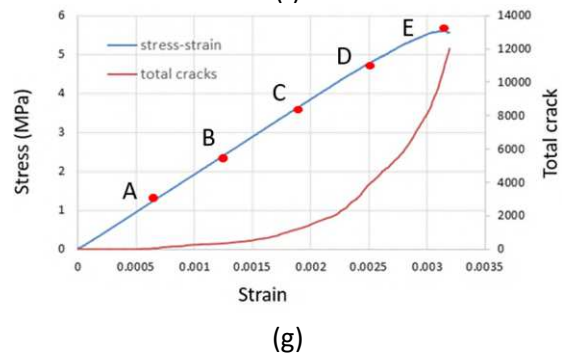
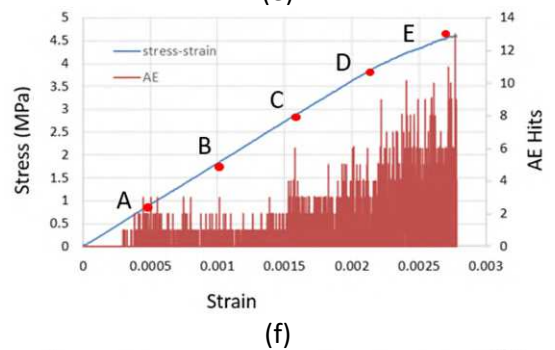
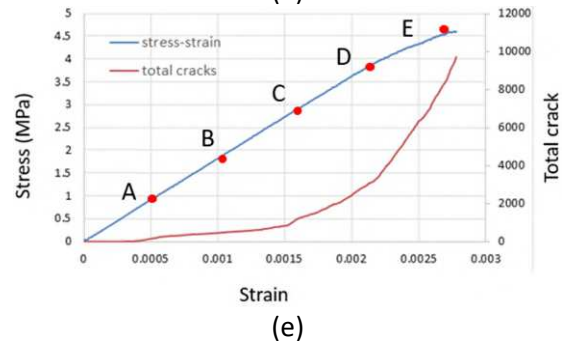
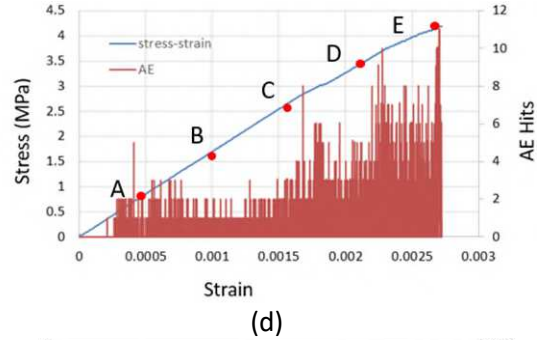
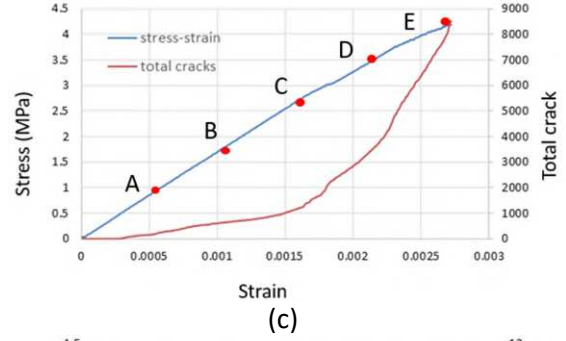
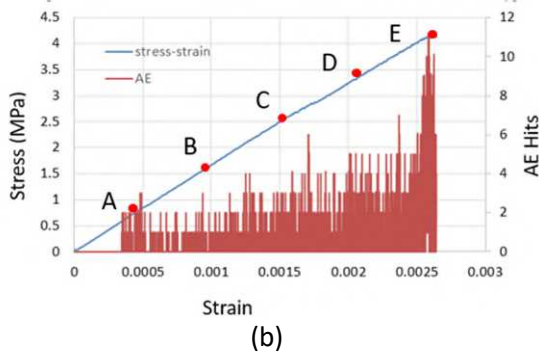
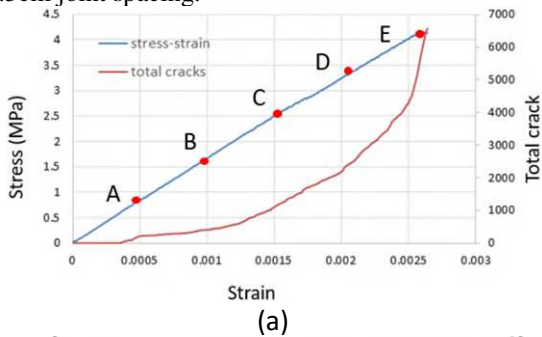


Fig 20 Ross diagram of crack growth for F shape joint with angle of; a) 0, b) 30, c) 60, d) 90.

Fig. 21 a, c, e, g shows the stress-strain curve along with the total crack number, and Fig. 21 b, d, f, h depicts the stress-strain curve along with AE hits. Along the stress-strain curve, five points labeled A-E were marked, and the stress at each point are 20%, 40%, 60%, 80% and 100% of total stress, respectively. The corresponding points were also marked in Fig. 21 b, d, f, h. It showed that before point C in the simulation there weren't any AE hits before point C in the simulation. It is important to note that increasing the number of AE events leads to increasing specimen loading. During stage CD, the deformation of the model showed linear elastic behavior and the number of AE hits increased gradually. Then, the curve turns to non-linear form, the increment of AE hits stepped-up, afterward the applied force reached to its peak and cracks integrated. In addition, before the peak load, there was a little fluctuation, subsequently there was a trough in the number of AE hits (Fig. 18 b, d, f, h), which related to the slowly growing of the crack number before the peak load in Fig. 21 a, c, e, g. After the peak load (point E) stress decreases greatly and it is due to the macro-failure throughout the model, indeed the small stress drop is also accompanied by a large amount of AE hits. Thus, an unreal conclusion is drawn that each stress drop during steady loading will cause to the emergence of large amount of AE hits. The evolution process of AE hits is similar to that of 1.5cm joint spacing.



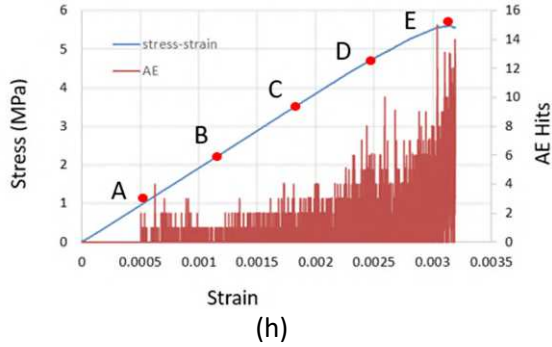


Fig. 21. Stress and AE behavior in the test simulation for joint spacing of 3m, a) stress-strain curve and cumulative crack number for joint angle of 0, b) the number of AE hits along the strain curve for joint angle of 0, c) stress-strain curve and cumulative crack number for joint angle of 30, d) the number of AE hits along the strain curve for joint angle of 30, e) stress-strain curve and cumulative crack number for joint angle of 60, f) the number of AE hits along the strain curve for joint angle of 60, g) stress-strain curve and cumulative crack number for joint angle of 90, h) the number of AE hits along the strain curve for joint angle of 90.

c) Distance between small joints was 4.5 cm

Fig. 22 depicts the failure pattern of samples with large joint angle of 0, 30, 60, and 90. The green line and red line are representative of tensile crack and shear crack, respectively. Fig 23 depicts Ross diagram of crack growth. When the angle of large joint was 0 (Fig. 22a), two tensile wing cracks originated from large joint and distributed parallel to loading axis till integrated with boundaries of specimen. One of the vertical small joint was mobilized in failure process. When the angle of large joint was 30 (Fig. 22b), two tensile wing cracks originated from both of the large joint and small joint and distributed parallel to loading axis till integrated with boundaries of specimen. Rock bridge failure was occurred by two oriented tensile cracks. When the angle of large joint was 60 (Fig. 22c), two tensile wing cracks originated from large joint and distributed parallel to loading axis till integrated with boundaries of specimen. One of the small joint was mobilized in failure process. Rock bridge failure was occurred by one oriented tensile cracks. When the angle of large joint was 90 (Fig. 22d), two tensile wing cracks originated from small joints and distributed parallel to loading axis till integrated with boundaries of specimen.

From Fig 23, the angles of micro cracks varied from 75 to 105 degree. The increasing of joint angle has not any effect on the newborn crack numbers.

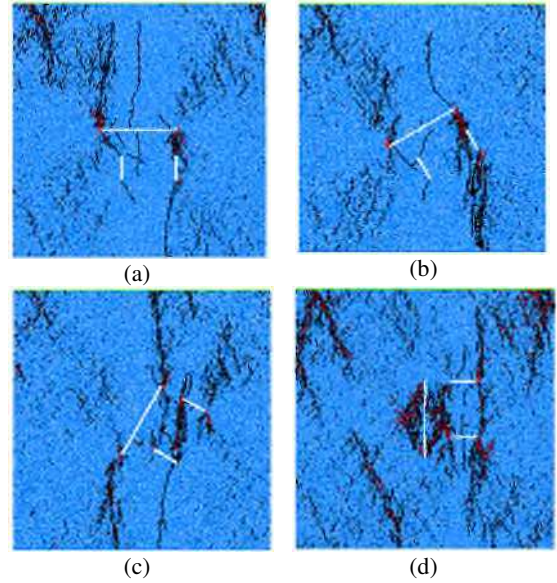
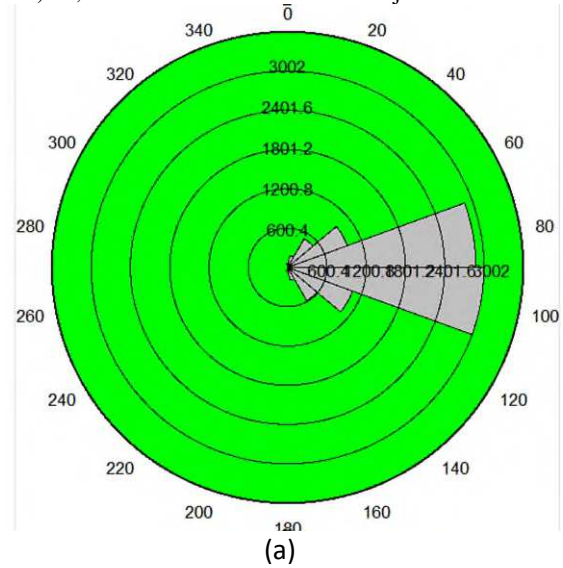


Fig 22. Crack pattern in specimen containing F shape non persistent joints with large joint angle of; a) 0, b) 30, c) 60, d) 90; vertical distance between small joint was 4cm.



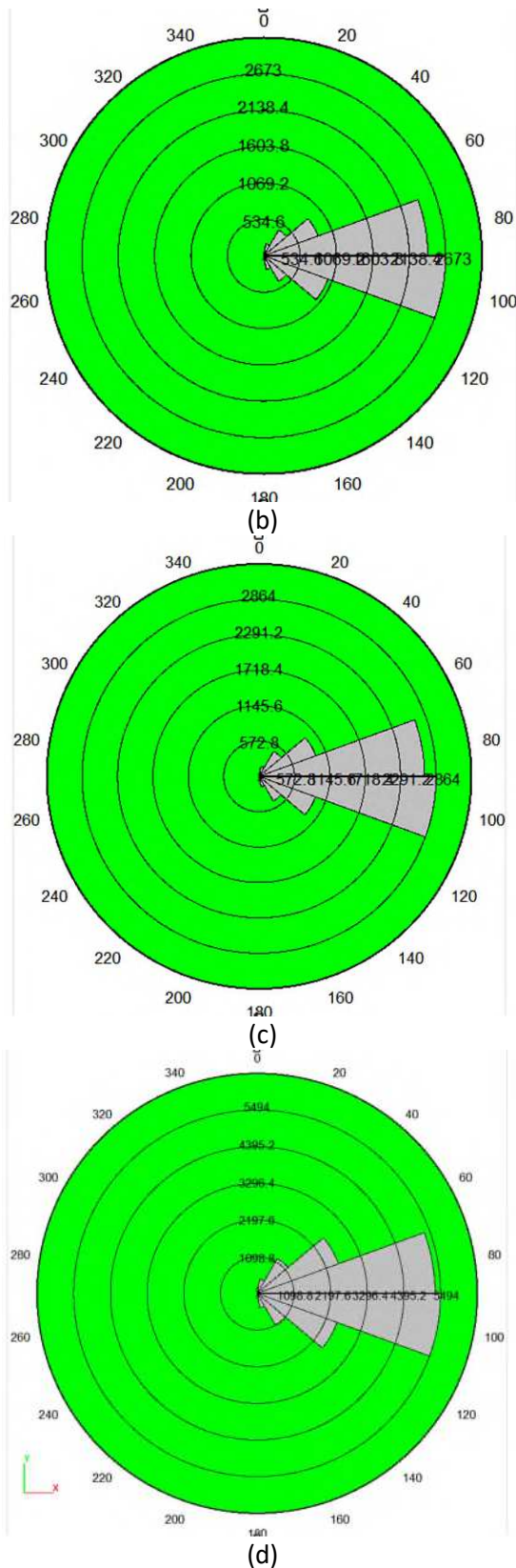
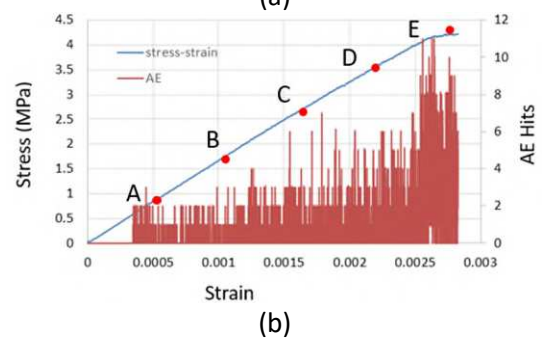
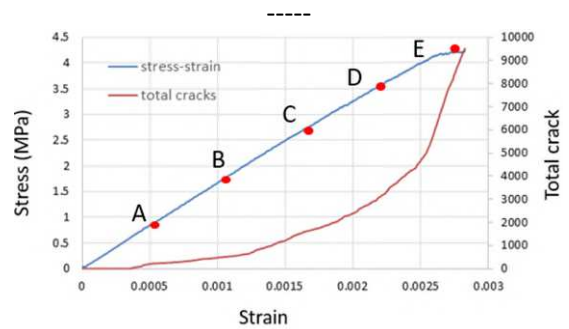
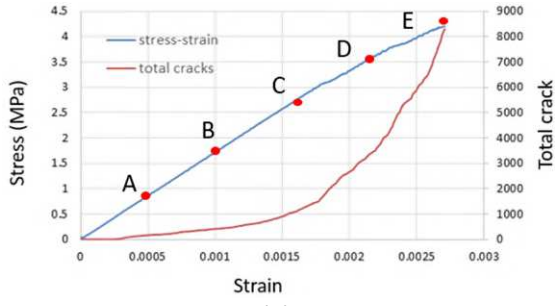


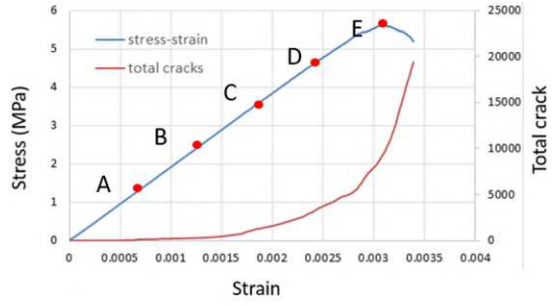
Fig 23 Ross diagram of crack growth for F shape joint with angle of; a) 0, b) 30, c) 60, d) 90.

Fig. 24 a, c, e, g shows the stress-strain curve along with the total number of cracks, and Fig. 24 b, d, f, h shows the stress-strain curve along with AE hits. Along the stress-strain curve, five points labeled A-E were marked, and the stress at each point are 20%, 40%, 60%, 80% and 100% of total stress, respectively. The corresponding points were also marked in Fig. 24 b, d, f, h. It showed that there weren't any AE hits before point C in the simulation. It's important to note that increasing the number of AE events leads to increasing loading of sample. During stage CD, the deformation of the model showed linear elastic behavior and the number of AE hits increased gradually. Then, the curve became non-linear, the increment of AE hits stepped-up, afterward the applied force reached to its peak and cracks integrated. Before the peak load, there was a small fluctuation, subsequently was a trough in the number of AE hits (Fig. 24 b, d, f, h), which is because of slow growing of the crack number before the peak load in Fig. 24 a, c, e, g. Macro-failure throughout the model leads to the large stress drops after the peak load (point E), actually the small stress drop is also accompanied by a large amount of AE hits. However, an unreal conclusion is drawn that each stress drop during steady loading will lead to the emergence of large amount of AE hits. The evolution process of AE hits is similar to that of 1.5cm joint spacing.

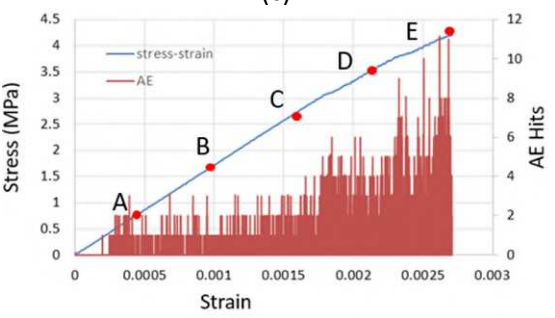




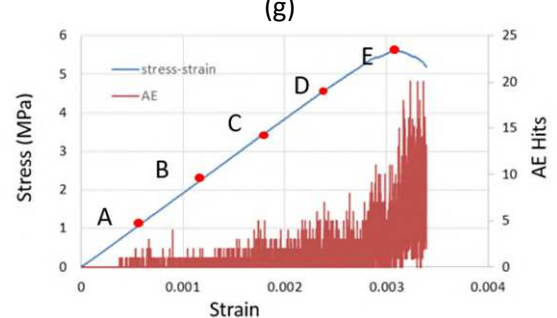
(c)



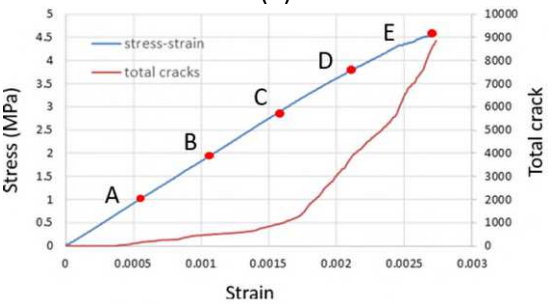
(g)



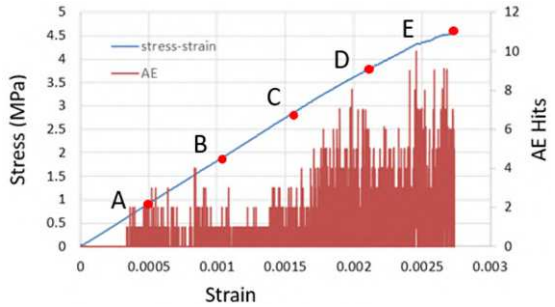
(d)



(h)



(e)



(f)

Fig. 24. Stress and AE behavior in the test simulation for joint length of 6cm, a) stress-strain curve and cumulative crack number for joint angle of 0, b) the number of AE hits along the strain curve for joint angle of 0, c) stress-strain curve and cumulative crack number for joint angle of 30, d) the number of AE hits along the strain curve for joint angle of 30, e) stress-strain curve and cumulative crack number for joint angle of 60, f) the number of AE hits along the strain curve for joint angle of 60, g) stress-strain curve and cumulative crack number for joint angle of 90, h) the number of AE hits along the strain curve for joint angle of 90.

By comparison between Figs 7-9 and Figs 16, 19 and 22, It can be concluded that failure pattern is identical in both of the experimental test and numerical simulation.

4.5 The influence of joint spacing and joint angle on the strength of samples

Fig 25 shows the influence of joint angle on the strength of models. This figure was presented for three joint spacing. The strength of specimens was increased by increasing the joint spacing. The minimum of compressive strength occurs when joint angle was 30. In fact, when large joint angle was 30, all notches were mobilized in failure process so the compressive strength will be decreased.

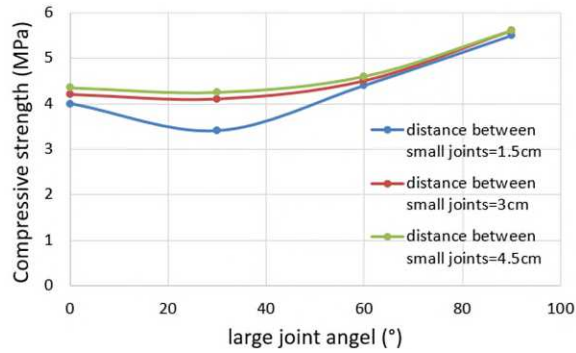


Fig 25 the influence of joint angle on the strength of models.

By comparison between Fig 10 and Fig 25 It can be concluded that failure strength is nearly identical in both of the experimental test and numerical simulation.

5. Conclusion

Experimental and discrete element approaches were used to investigate the effects of F shape non-persistent joints on the failure behaviour of concrete under uniaxial compressive test. concrete specimens with dimensions of 200 mm×200 mm×50 mm were provided. Within the specimen, F shape non-persistent joint consisting three joints were provided. The large joint length was 6 cm, and the length of two small joints were 2cm. Vertical distance between two small joints change from 1.5 cm to 4.5 cm with increment of 1.5 cm. In constant joint lengths, the angle of large joint change from 0 to 90 with increments of 30. Totally 12 different models were tested under compression test. The axial load rate on the model was 0.05 mm/min. Concurrent with experimental tests, numerical simulation (Particle flow code in two dimension) were performed on the models containing F shape non-persistent joint. Distance between small joints and joint angles were similar to experimental one. the results showed that the results show that:

- *Distance between small joints was 1.5 cm*

When the angle of large joint was 0, two tensile wing cracks originated from large joint and distributed parallel to loading axis till integrated with boundaries of specimen. One of the vertical small joint was mobilized in failure process. Rock bridge failure was occurred by two tensile cracks. When the angle of large joint was 30, two tensile wing cracks originated from both of the large joint and small joint and distributed parallel to loading axis till integrated with boundaries of sample. Rock bridge failure was occurred by two tensile cracks. When the angle of large joint was 60, two tensile wing cracks originated from both of the large joint and small joint and distributed parallel to loading axis till integrated with boundaries of specimen. Also, rock bridges were broken by two oriented wing cracks. When the angle of large

joint was 90, two tensile wing cracks originated from small joints and distributed parallel to loading axis till integrated with boundaries of specimen. The large joint has not any effect in failure process.

- *Distance between small joints was 3 cm*

When the angle of large joints was 0 and 30, two tensile wing cracks originated from large joint and distributed parallel to loading axis till integrated with boundaries of specimen. One of the small joint was mobilized in failure process. When the angle of large joint was 60, two tensile wing cracks originated from both of the large joint and small joint and distributed parallel to loading axis till integrated with boundaries of sample. Also, rock bridges were broken by two oriented wing cracks. When the angle of large joint was 90, two tensile wing cracks originated from small joints and distributed parallel to loading axis till integrated with boundaries of specimen. The large joint has not any effect in failure process.

- *Distance between small joints was 4.5 cm*

When the angle of large joint was 0, two tensile wing cracks originated from large joint and distributed parallel to loading axis till integrated with boundaries of specimen. One of the vertical small joint was mobilized in failure process. When the angle of large joint was 30, two tensile wing cracks originated from both of the large joint and small joint and distributed parallel to loading axis till integrated with boundaries of specimen. Rock bridge failure was occurred by two oriented tensile cracks. When the angle of large joint was 60, two tensile wing cracks originated from large joint and distributed parallel to loading axis till integrated with boundaries of specimen. One of the small joint was mobilized in failure process. Rock bridge failure was occurred by one oriented tensile cracks. When the angle of large joint was 90, two tensile wing cracks originated from small joints and propagated parallel to loading axis till integrated with boundaries of sample.

- The angles of micro cracks varied between 75 and 105 degrees.
- The minimum of compressive strength occurs when triple joint angle was 30.
- The strength of sample was increased by increasing the joint spacing.
- When the small joint angles were 0 and 90, the AE hits was in a slowly increasing trend. When the small joint angle is 30 and 60, the second stage of AE hits does not increase slowly, but there are multiple peaks, which is caused by the continuous step expansion of the cracks. This shows that the crack

propagation and penetration mechanism and mode of jointed rock specimens are greatly affected by the increase of joint length. Joint angle changes the failure mode of jointed rock sample, and has important effect on the evolution of AE.

- In both the numerical simulation and experimental test, the failure pattern is identical.
- In both the numerical simulation and experimental test, the failure strength is identical.

References

- Ashby MFA, Hallam SD (1986) The failure of brittle solids containing small cracks under compressive stress states. *Acta Metall Sin* 34(3):497–510
- Bagher Shemirani A., Amini M.S., Sarfarazi, V. (2021) Experimental and numerical investigation of the effect of bridge area and its angularities on the failure mechanism of non-persistent crack in concrete-like materials. *Smart Structures and Systems, An Int'l Journal* Vol. 27(3):54-67.
- Baud P, Reuschle T, Charlez P (1996) An improved wing crack model for the deformation and failure of rock in compression. *Int J Rock Mech Min Sci* 33(5):539–542
- Bobet A, Einstein HH (1998a) Numerical modeling of fracture coalescence in a model rock material. *Int J Fract* 92:221–252
- Bobet A, Einstein HH (1998b) Fracture coalescence in rock-type materials under uniaxial and biaxial compression. *Int J Rock Mech Min Sci* 35(7):863–888
- Barenblatt GI (1962) The mathematical theory of equilibrium of cracks in brittle fracture. *Adv Appl Mech* 7:55–129
- Cao Rihong, Yao Rubing, Meng JingJing, Lin Qibin*, Lin Hang, Li Su. Failure mechanism of non-persistent jointed rock-like specimens under uniaxial loading: Laboratory testing[J]. *International Journal of Rock Mechanics and Mining Sciences*, 2020, 132, 10434.
- Cheng X., (2019) Damage and failure characteristics of rock similar materials with pre-existing cracks, *Int J Coal Sci Technol* 6(4):505–517
- Dugdale DS (1960) Yielding of steel sheets containing slits. *J Mech Phys Solids* 8:100–104. 18. Gonçalves da Silva B, Einstein HH (2013) Modeling of crack initiation, propagation and coalescence in rocks. *Int J Fract* 182:167–186
- Ghazvinian, A., Sarfarazi, V., Schubert, W. and Blumel, M. (2012), “A study of the failure mechanism of planar non-persistent open joints using PFC2D”, *Rock Mech. Rock Eng.*, 45(5), 677-693. <https://doi.org/10.1007/s00603-012-0233-2>.
- Griffith AA (1920) The phenomenon of rupture and flow in solids. *Philos Trans R Soc Lond Ser A* 221:163–198
- Hoek E (1964) Fracture of anisotropic rock. *J S Afr Inst Min Metall* 64(10):501–518
- Hoek E, Bieniawski ZT (1965) Brittle fracture propagation in rock under compression. *J Fract Mech* 1(3):139–155
- Haeri, H. and Sarfarazi, V. (2019) Experimental and numerical studies of the pre-existing cracks and pores interaction in concrete specimens under compression. *Smart Structures and Systems, An Int'l Journal* Vol. 23(5):47-59.
- Hu Jianhua, Wen Guanping, Lin Qibin*, Cao Ping, Li Su. Mechanical properties and crack evolution of double-layer composite rock-like specimens with two parallel fissures under uniaxial compression[J]. *Theoretical and Applied Fracture Mechanics*, 2020, 108, 102610.
- Hillerborg A, Modeer M, Petersson PE (1976) Analysis of crack formation and crack growth in concrete by means of fracture mechanics and finite elements. *Cem Concr Res* 6:773–782
- Horri H, Nemat-Naseer S (1985) Compression-induced microcrack growth in brittle solids: axial splitting and shear failure. *J Geophys Res* 90(B4):3105–3125
- Inglis CE (1913) Stresses in a plate due to the presence of cracks and sharp corners. *Trans Inst Nav Archit* 60:219–230
- Kou, M.; Liu, X.; Tang, S.; Wang, Y. 3-D X-ray computed tomography on failure characteristics of rock-like materials under coupled hydro-mechanical loading. *Theor. Appl. Fract. Mech.* 2019, 104, 102396.
- Lin Qibin, Cao Ping, Cao Rihong, Lin Hang, Meng Jingjing. Mechanical behavior around double circular openings in a jointed rock mass under uniaxial compression[J]. *Archives of Civil and Mechanical Engineering*. 2020, 20(1), 19.
- Lisjak A, Figi D, Grasselli G (2014) Fracture development around deep underground excavations: insights from FDEM modelling. *J Rock Mech Geotech Eng* 6:493–505
- Lee H, Jeon S (2011) An experimental and numerical study of fracture coalescence in pre cracked specimens under uniaxial compression. *Int J Solids Struct* 48(6):979–999
- Lin Qibin, Cao Ping, Meng Jingjing, Cao Rihong, Zhao Zhiye. Strength and failure characteristics of jointed rock mass with double circular holes under uniaxial compression: Insights from discrete element method modelling[J]. *Theoretical and Applied Fracture Mechanics*. 2020, 109, 102692.
- Mahabadi OK, Lisjak A, Grasselli G, Munjiza A (2012) Y-Geo: a new combined finite-discrete element numerical code for geomechanical applications. *Int J Geomech* 12(6):676–688
- Miao, S.; Pan, P.-Z.; Wu, Z.; Li, S.; Zhao, S. Fracture analysis of sandstone with a single filled flaw under uniaxial compression. *Eng. Fract. Mech.* 2018, 204, 319–343.
- Orowan E (1949) Fracture and strength of solids. *Rep Progr Phys* 12:185–232
- Potyondy, D. O. (2012). A flat-jointed bonded-particle material for hard rock. Paper presented at the 46th U.S. Rock Mechanics/Geomechanics Symposium, Chicago, USA.
- Potyondy, D. O. (2015). The bonded-particle model as a tool for rock mechanics research and application: Current trends and future directions. *Geosystem Engineering*, 18(1), 1–28. doi:10.1080/12269328.2014.998346
- Potyondy, D.O., Cundall, P.A., 2004. A bonded-particle model for rock. *International Journal of Rock Mechanics and Mining Sciences* 41, 1329–1364.

- Potyondy, D. O. (2017). Simulating perforation damage with a flat-jointed bonded-particle material. Paper presented at the 51st US Rock Mechanics/Geomechanics Symposium, San Francisco, California, USA.
- Park CH, Bobet A (2009) Crack coalescence in specimens with open and closed flaws: a comparison. *Int J Rock Mech Min Sci* 46(5):819–829
- Park CH, Bobet A (2010) Crack initiation, propagation and coalescence from frictional flaws in uniaxial compression. *Eng Fract Mech* 77(14):2727–2748.
- Qian, X.K.; Liang, Z.Z.; Liao, Z.Y.; Wang, K. Numerical investigation of dynamic fracture in rock specimens containing a pre-existing surface flaw with different dip angles. *Eng. Fract. Mech.* 2020, 223, 106675.
- Reyes O, Einstein HH (1991) Failure mechanism of fractured rock—a fracture coalescence model. In: *Proceedings of the 7th congress of the ISRM, Aachen, Germany, vol 1*, pp 333–340
- Steif PS (1984) Crack extension under compressive loading. *Eng Fract Mech* 20(3):463–473
- Sarfarazi, V., Ghazvinian, A., Schubert, W., Blumel, M. and Nejati, H.R. (2014), “Numerical simulation of the process of fracture of Echelon rock joints”, *Rock Mech. Rock Eng.*, 47(4), 1355-1371. DOI: [10.1007/s00603-013-0450-3](https://doi.org/10.1007/s00603-013-0450-3)
- Sarfarazi, V. and Haeri, H., (2016a), “Effect of number and configuration of bridges on shear properties of sliding surface”, *J. Min. Sci.*, 52(2), 245-257. <https://doi.org/10.1134/S1062739116020370>
- Sarfarazi, V., Faridi, H.R., Haeri, H. and Schubert, W. (2016b), “A new approach for measurement of anisotropic tensile strength of concrete”, *Adv. Concrete Constr.*, 3(4), 269-284. DOI: <http://dx.doi.org/10.12989/acc.2015.3.4.26>
- Sarfarazi, V., Haeri, H. and Khaloo, A. (2016c), “The effect of non-persistent joints on sliding direction of rock slopes”, *Comput. Concrete*, 17(6), 723-737. DOI: [10.12989/cac.2016.17.6.723](https://doi.org/10.12989/cac.2016.17.6.723).
- Sagong M, Bobet A (2002) Coalescence of multiple flaws in a rock- model material in uniaxial compression. *Int J Rock Mech Min Sci* 39(2):229–241
- Vasarhelyi B, Bobet A (2000) Modeling of crack initiation, propagation and coalescence in uniaxial compression. *Rock Mech Min Sci* 33(2):119–139.
- Wong LNY, Einstein HH (2009a) Crack coalescence in molded gypsum and Carrara marble: part 1—macroscopic observations and interpretation. *Rock Mech Rock Eng* 42(3):475–511
- Wong LNY, Einstein HH (2009b) Systematic evaluation of cracking behavior in specimens containing single flaws under uniaxial compression. *Int J Rock Mech Min Sci* 46(2):239–249
- Wu, S., & Xu, X. (2016). A study of three intrinsic problems of the classic discrete element method using flat-joint model. *Rock Mechanics and Rock Engineering*, 49(5), 1813–1830. doi:10.1007/s00603-015-0890-z
- Wu, Q.H.; Li, X.B.;Weng, L.; Li, Q.F.; Zhu, Y.J.; Luo, R. Experimental investigation of the dynamic response of prestressed rockbolt by using an SHPB-based rockbolt test system. *Tunn. Undergr. Sp. Technol.* 2019, 93,103088.
- Xu Y, Yuan H (2011) Applications of normal stress dominated cohesive zone models for mixed-mode crack simulation based on extended finite element methods. *Eng Fract Mech* 78:544–558
- Xie Y, Cao P, Liu J, Dong L (2016) Influence of crack surface friction on crack initiation and propagation: a numerical investigation based on extended finite element method. *Comput Geotech* 74:1–14.
- Yang, S.Q.; Yang, Z.; Zhang, P.C.; Tian,W.L. Experiment and peridynamic simulation on cracking behavior of red sandstone containing a single non-straight fissure under uniaxial compression. *Theor. Appl. Fract. Mech.* 2020, 108, 102637.
- Yang, S.Q.; Huang, Y.H.; Ranjith, P.G. Failure mechanical and acoustic behavior of brine saturated-sandstone containing two pre-existing flaws under different confining pressures. *Eng. Fract. Mech.* 2018, 193, 108–121.
- Zhang, B.; Li, S.; Yang, X.; Xia, K.; Liu, J.; Guo, S.;Wang, S. The coalescence and strength of rock-like materials containing two aligned X- type flaws under uniaxial compression. *Geomech. Eng.* 2019, 17, 47–56.
- Zhou, T.; Zhu, J.B.; Ju, Y.; Xie, H.P. Volumetric fracturing behavior of 3D printed artificial rocks containing single and double 3D internal flaws under static uniaxial compression. *Eng. Fract. Mech.* 2019, 205, 190–204.
- Zhou, X.P.; Zhang, J.Z.;Wong, L.N.Y. Experimental Study on the Growth, Coalescence and Wrapping Behaviors of 3D Cross-Embedded Flaws Under Uniaxial Compression. *RockMech. Rock Eng.* 2018, 51, 1379–1400. [CrossRef]
- Zhou, X.P.; Li, G.Q.; Ma, H.C. Real-time experiment investigations on the coupled thermomechanical and cracking behaviors in granite containing three pre-existing fissures. *Eng. Fract. Mech.* 2020, 224, 106797.
- Zhang Q, Wang X, Tian L, et al. (2018) Analysis of mechanical and acoustic emission characteristics of rock materials with double-hole defects based on particle flow code. *Shock and Vibration*, 32(1):23-35.
- Zhou, X.P.; Li, L.H.; Berto, F. Cracking behaviors of rock-like specimens containing two sets of preexisting cross flaws under uniaxial compression. *J. Test. Eval.* 2019, 47, 838–867.
- Zhou, X.P.; Zhang, J.Z.; Yang, L.H.; Cui, Y.L. Internal morphology of cracking of two 3-d pre-existing cross-embedded flaws under uniaxial compression. *Geotech. Test. J.* 2018, 41, 20170189.
- Zhao, Y.L.; Zhang, L.Y.; Wang, W.J.; Wan, W.; Ma, W.H. Separation of elastoviscoplastic strains of rock and a nonlinear creep model. *Int. J. Geomech.* 2018, 18, 04017129.
- Zhao, Y.L.; Zhang, L.Y.; Wang, W.J.; Tang, J.Z.; Lin, H.; Wan, W. Transient pulse test and morphological analysis of single rock fractures. *Int. J. Rock Mech. Min. Sci.* 2017, 91, 139–154.
- Zhang X., (2020) Evaluation of structural safety reduction due to water penetration into a major structural crack in a large concrete project . *Smart Structures and Systems, An Int'l Journal* Vol. 26(3):90-108.

Figures

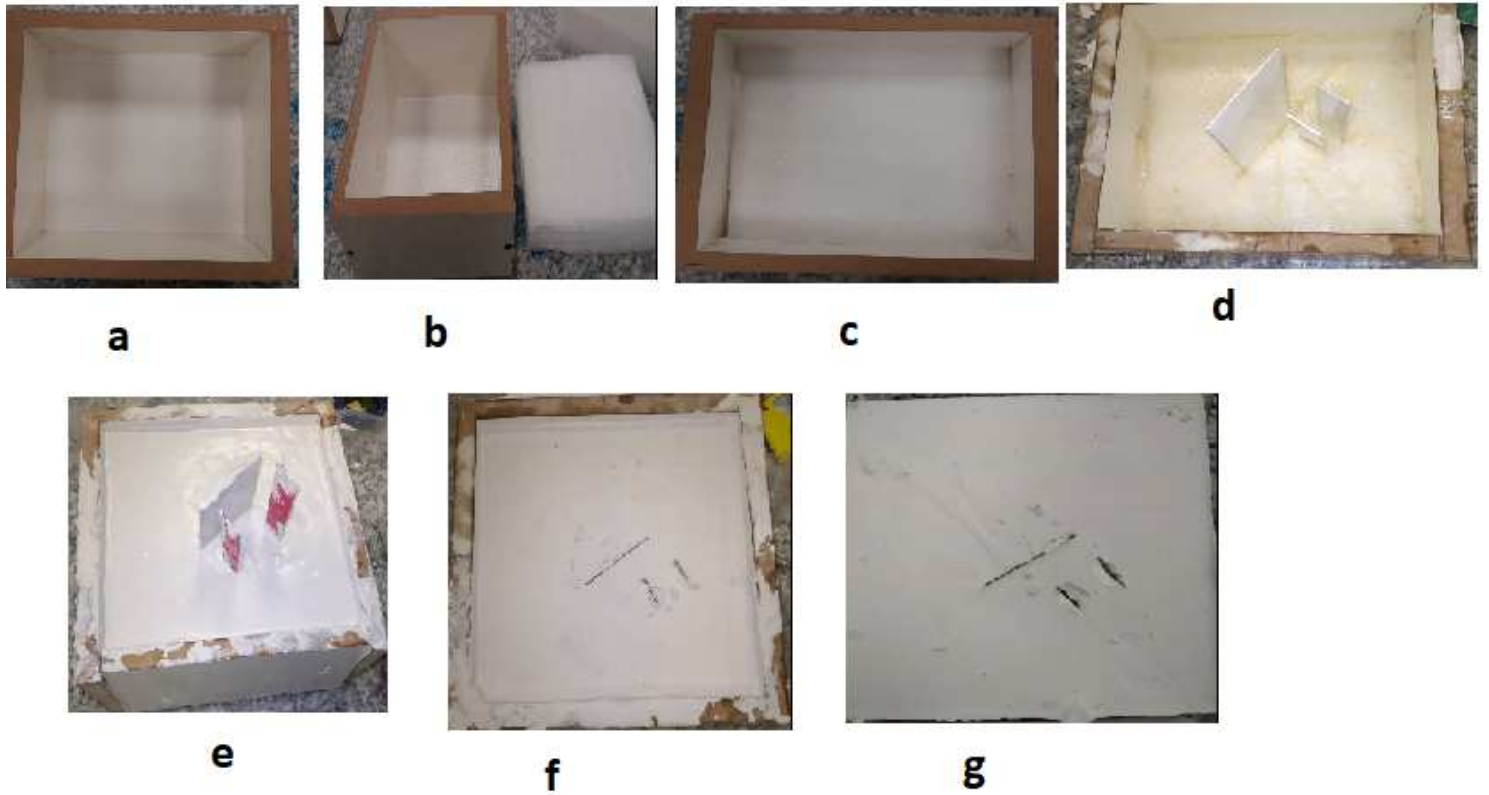


Figure 1

a) the frame with dimensions of 200mm× 200mm × 100mm, b and c) a unique plastic fiber with dimension of 200mm × 200 mm × 50 mm was put into the frame, d) the shim within the plastic fiber, e) slurry within the box, f) the aluminum sheet was taken out from the mold, g) the physical sample.

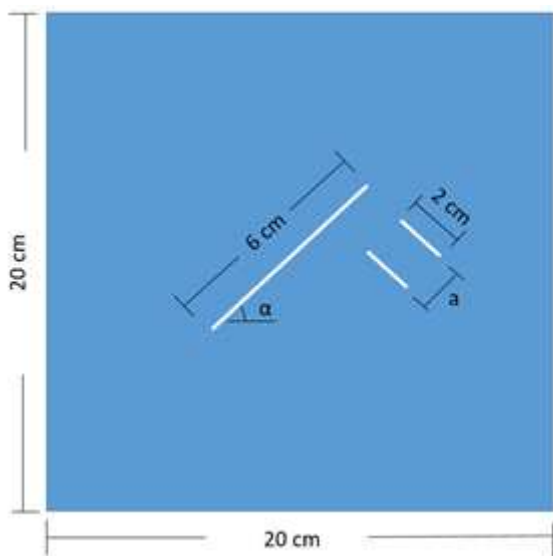


Figure 2

F shape non persistent joints

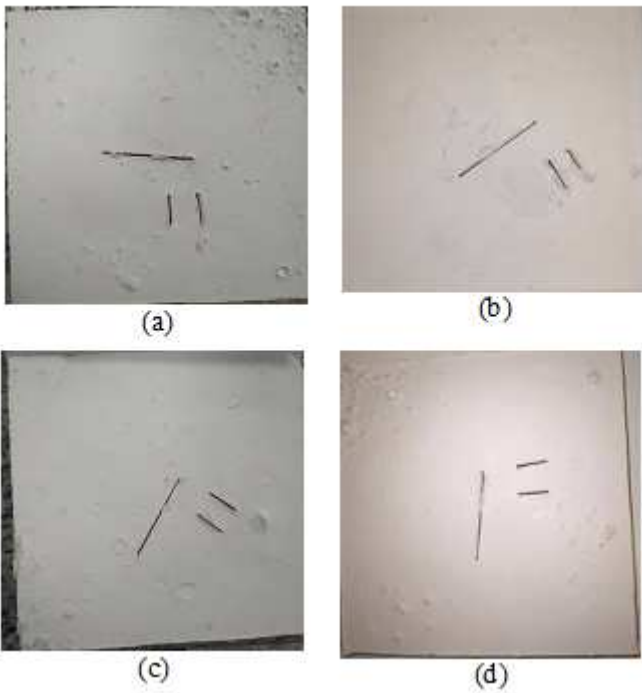


Figure 3

F shape non persistent joints with large joint angle of; a) 0, b) 30, c) 60, d) 90; vertical distance between small joint was 1.5cm.

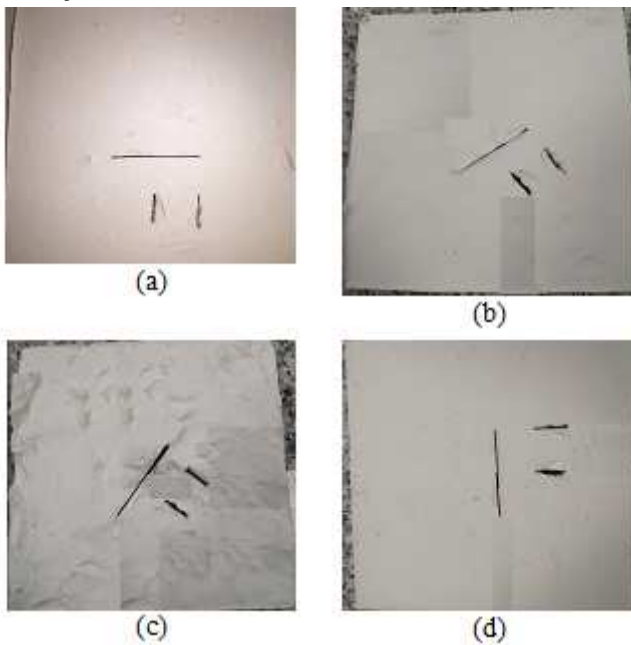


Figure 4

F shape non persistent joints with large joint angle of; a) 0, b) 30, c) 60, d) 90; vertical distance between small joint was 3cm.

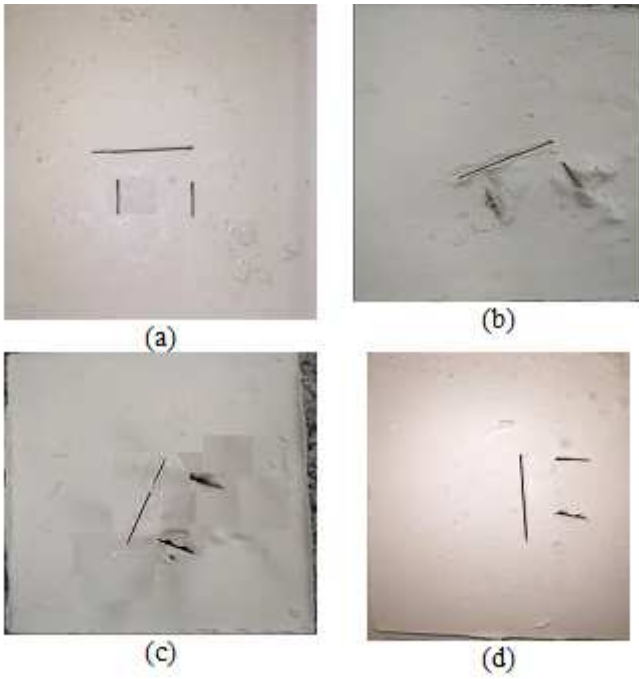


Figure 5

F shape non persistent joints with large joint angle of; a) 0, b) 30, c) 60, d) 90; vertical distance between small joint was 4cm.



Figure 6

Specimen are placed between the plates of the loading machine.

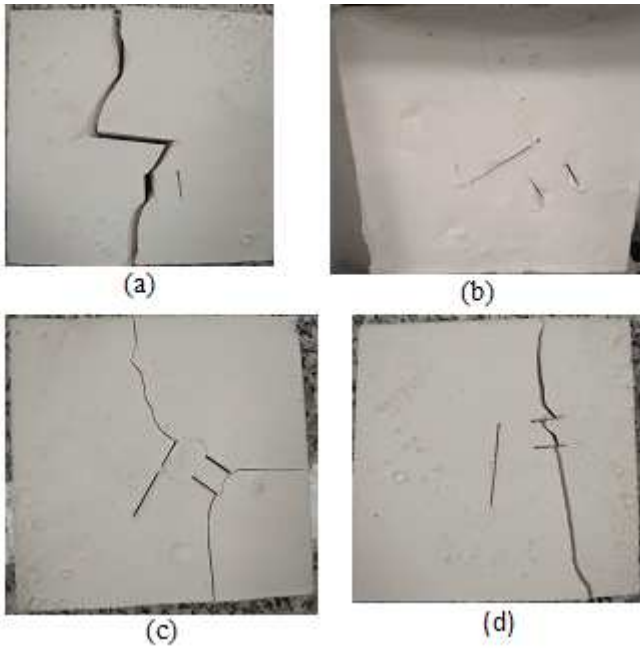


Figure 7

Failure pattern in F shape non persistent joints with large joint angle of; a) 0, b) 30, c) 60, d) 90; vertical distance between small joint was 1.5cm.

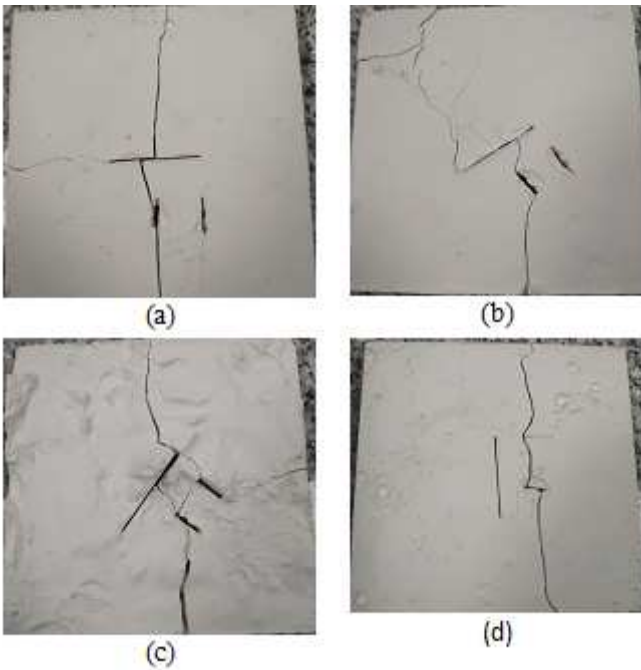


Figure 8

Failure pattern in F shape non persistent joints with large joint angle of; a) 0, b) 30, c) 60, d) 90; vertical distance between small joint was 3cm.

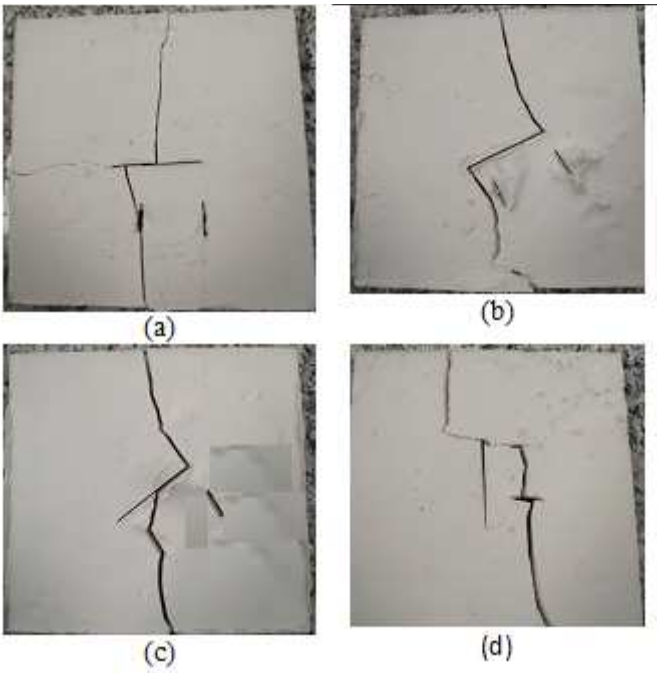


Figure 9

Failure pattern in F shape non persistent joints with large joint angle of; a) 0, b) 30, c) 60, d) 90; vertical distance between small joint was 4.5cm.

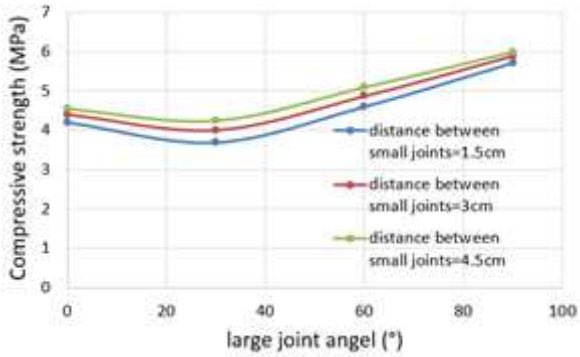


Figure 10

the influence of joint angle on the strength of models.

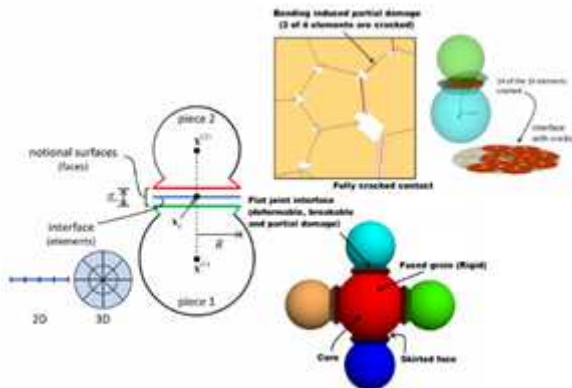


Figure 11

Flat-joint model (Potyondy, 2015).

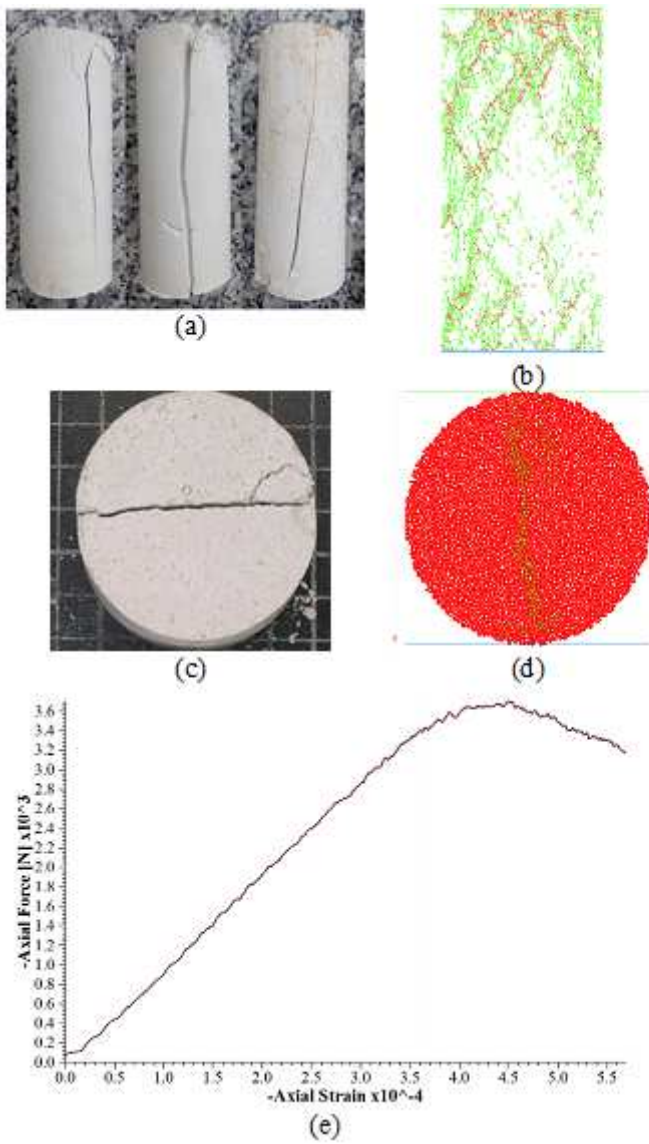


Figure 12

a) Experimental compression test, b) numerical compression test, c) experimental Brazilian test and d) numerical Brazilian test, e) axial force versus axial strain for numerical uniaxial compressive test

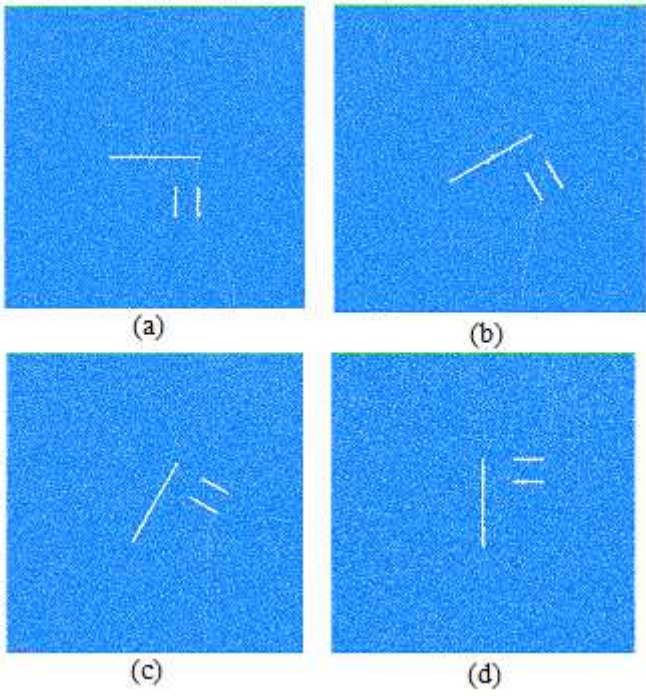


Figure 13

F shape non persistent joints with large joint angle of; a) 0, b) 30, c) 60, d) 90; vertical distance between small joint was 1.5cm.

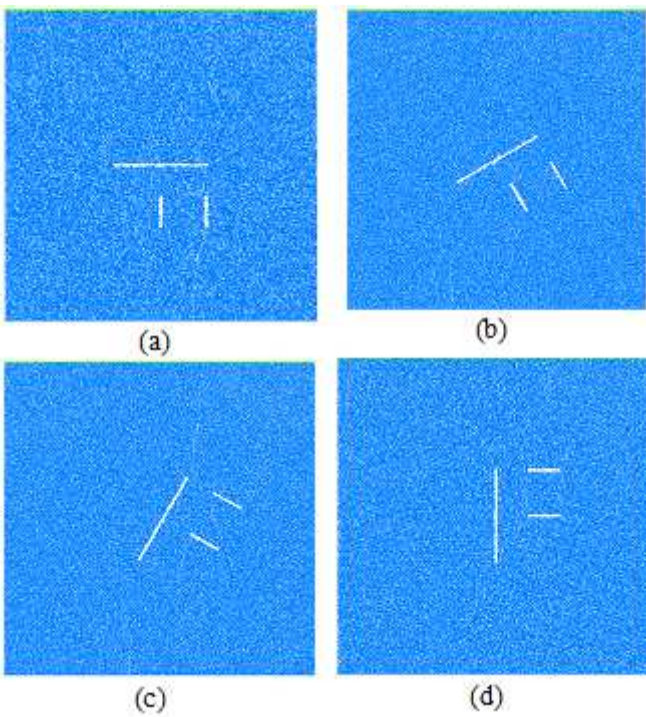


Figure 14

F shape non persistent joints with large joint angle of; a) 0, b) 30, c) 60, d) 90; vertical distance between small joint was 3cm.

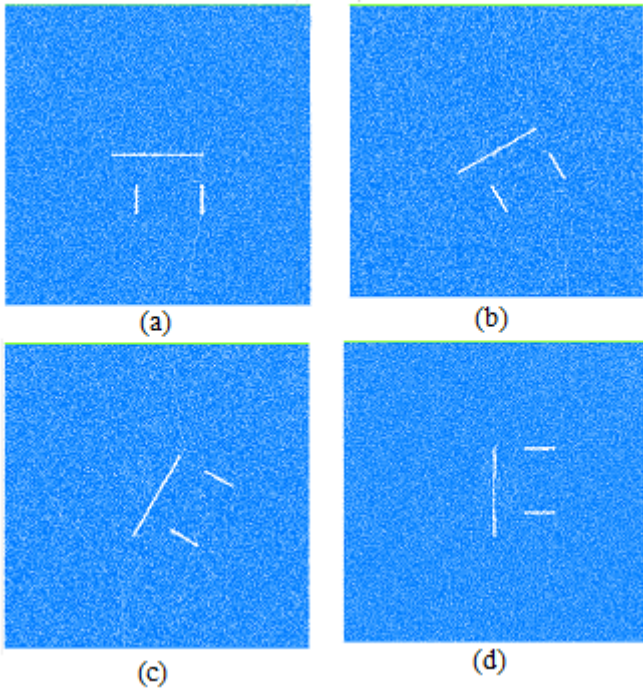


Figure 15

F shape non persistent joints with large joint angle of; a) 0, b) 30, c) 60, d) 90; vertical distance between small joint was 4.5cm.

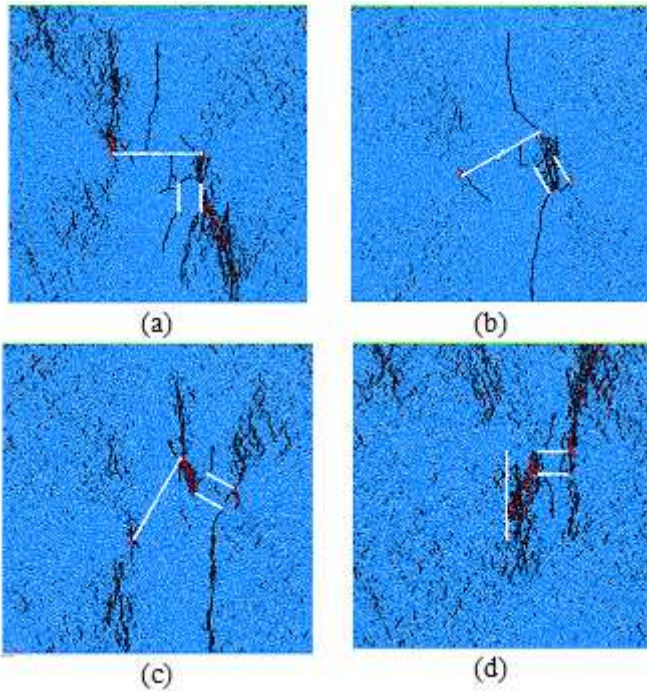
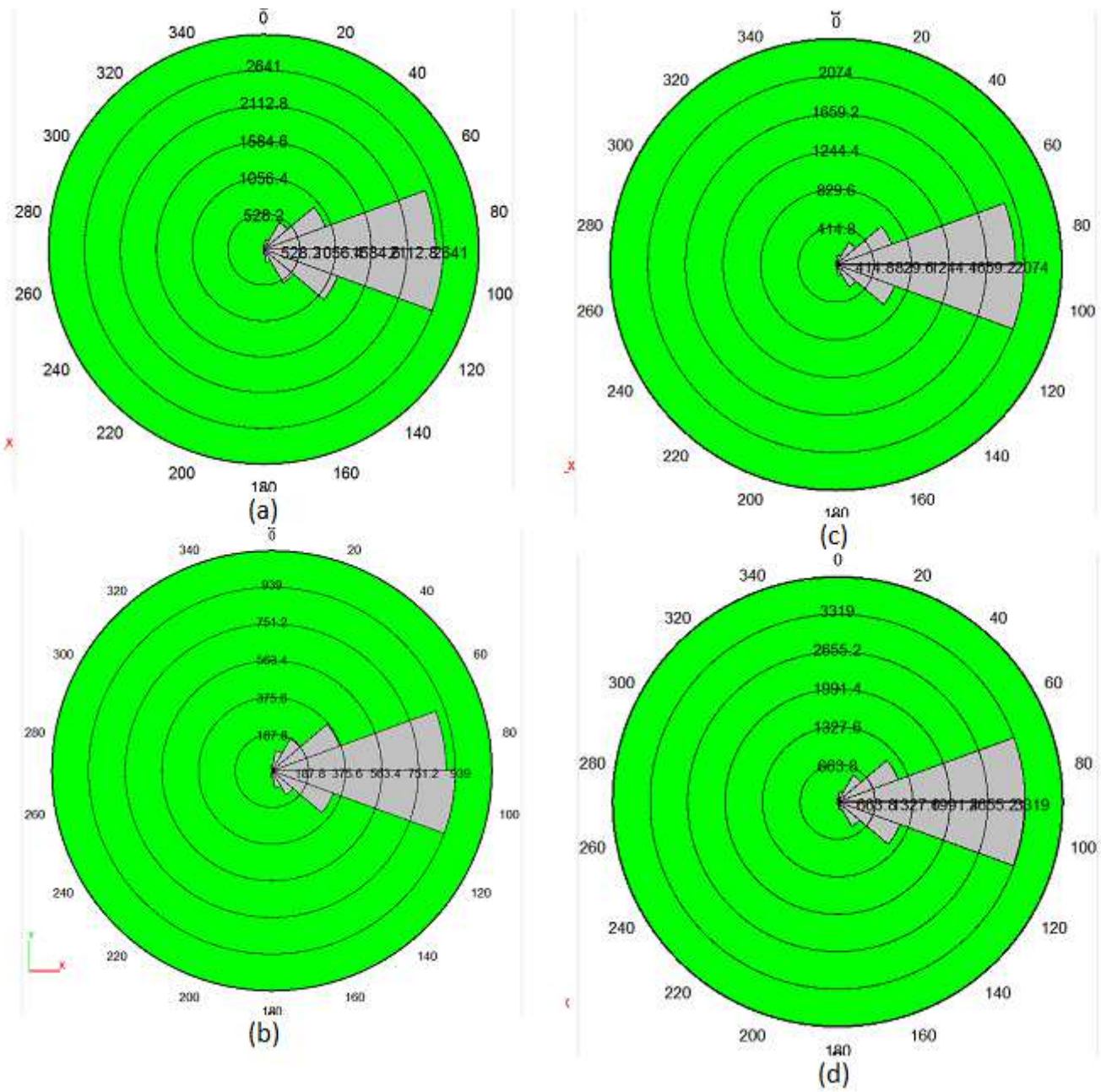


Figure 16

Crack pattern in specimen containing F shape non persistent joints with large joint angle of; a) 0, b) 30, c) 60, d) 90; vertical distance between small joint was 1.5cm.



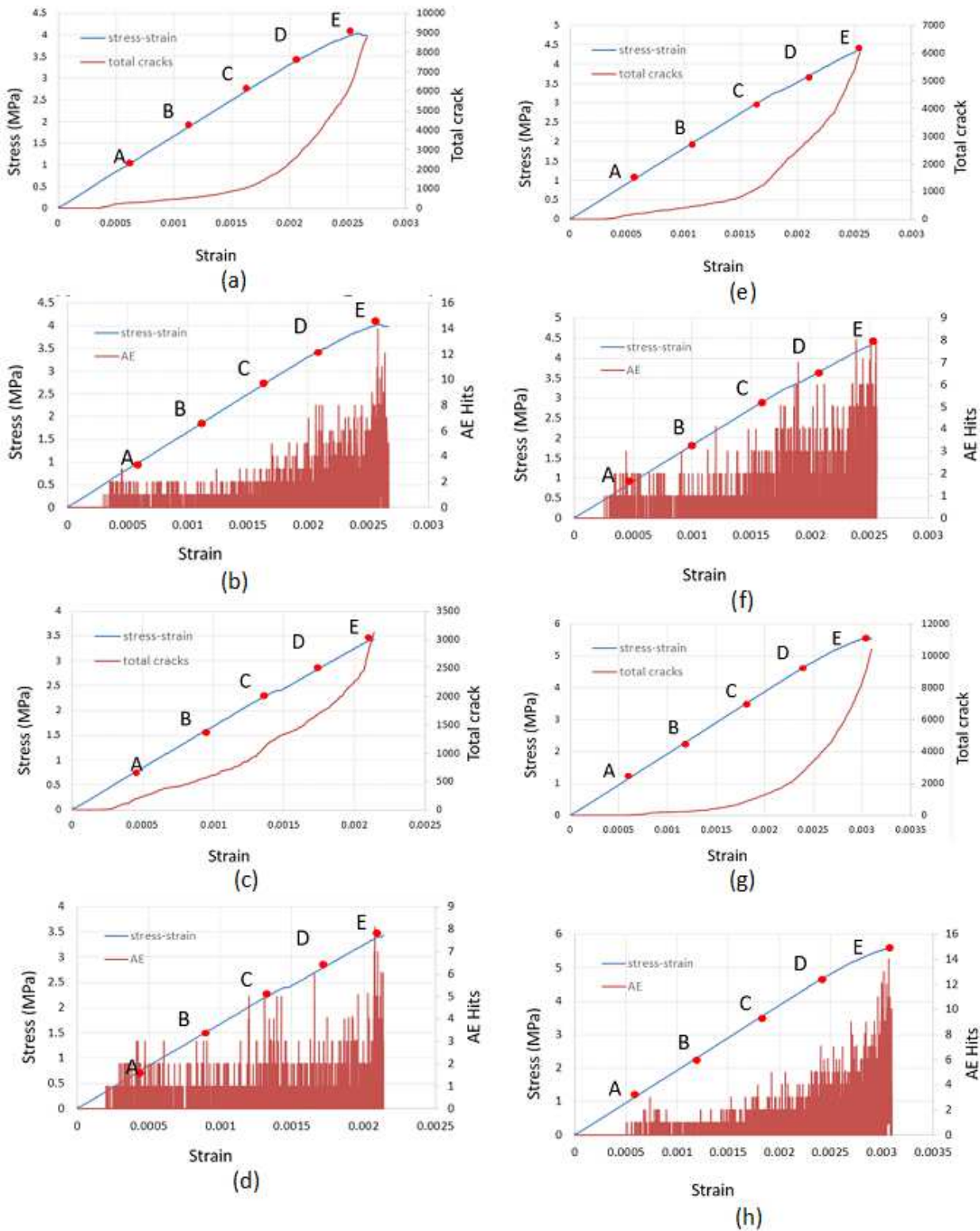


Figure 18

Stress and AE behavior in the test simulation for joint spacing of 1.5 cm, a) stress-strain curve and cumulative crack number for joint angle of 0, b) the number of AE hits along the strain curve for joint angle of 0, c) stress-strain curve and cumulative crack number for joint angle of 30, d) the number of AE hits along the strain curve for joint angle of 30, e) stress-strain curve and cumulative crack number for joint angle of 60, f) the number of AE hits along the strain curve for joint angle of 60, g) stress-strain

curve and cumulative crack number for joint angle of 90, h) the number of AE hits along the strain curve for joint angle of 90.

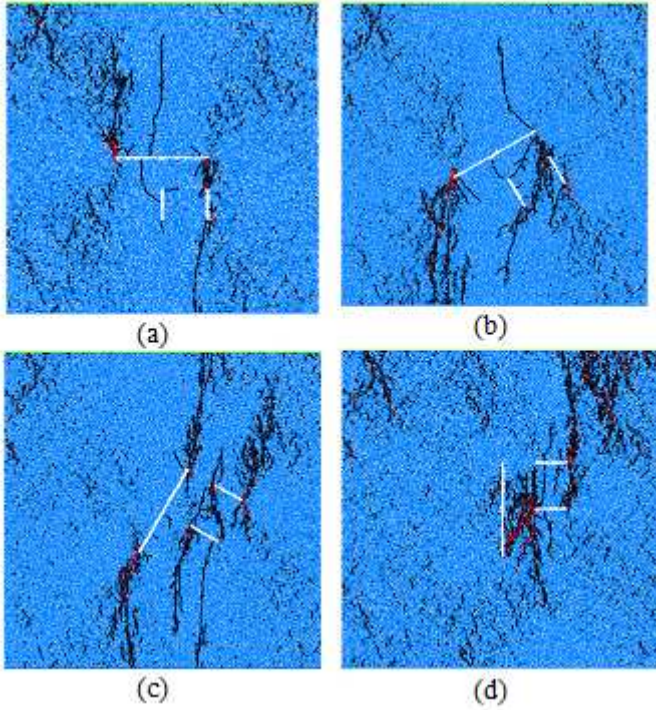


Figure 19

Crack pattern in specimen containing F shape non persistent joints with large joint angle of; a) 0, b) 30, c) 60, d) 90; vertical distance between small joint was 3cm.

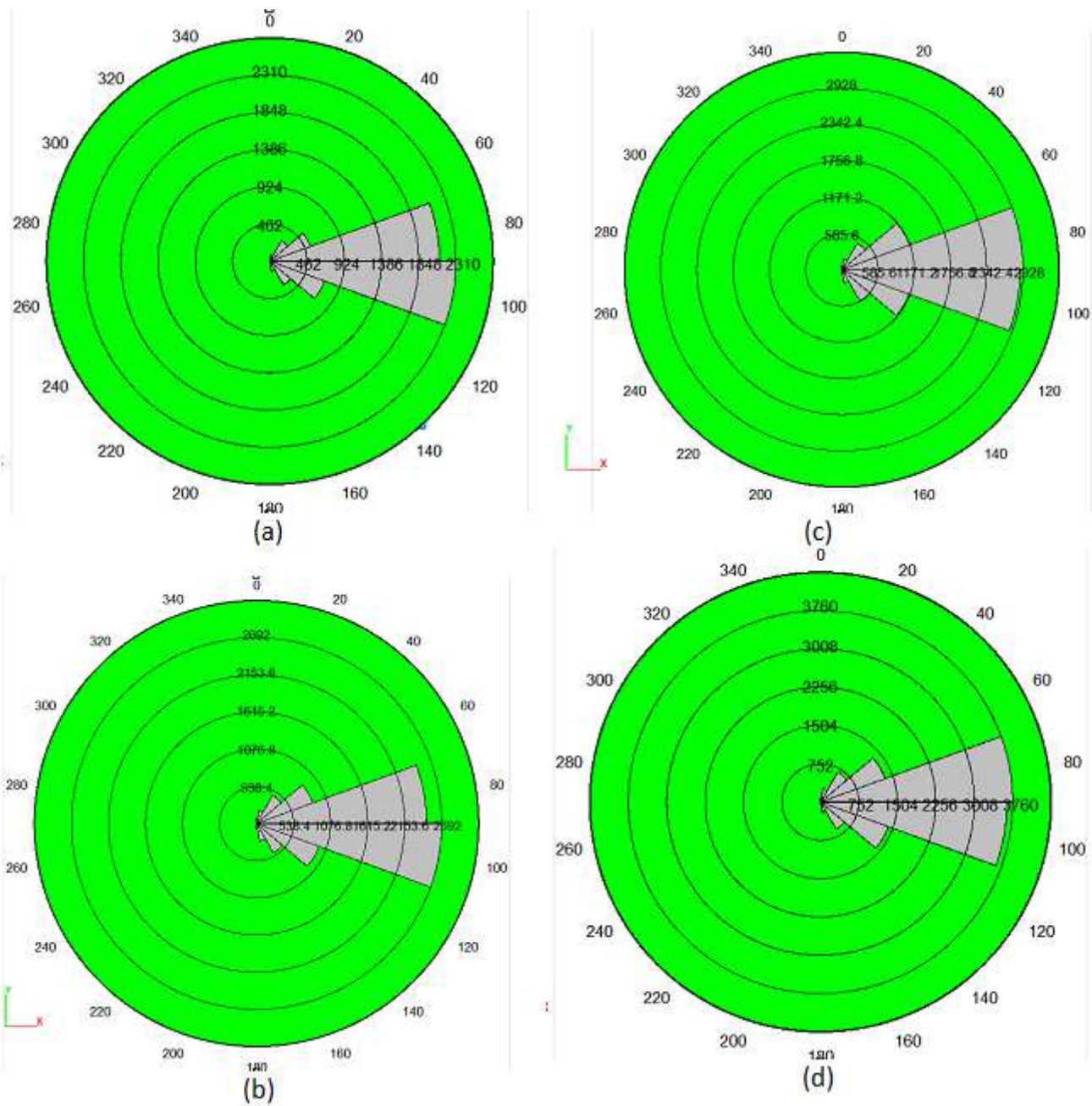


Figure 20

Ross diagram of crack growth for F shape joint with angle of θ ; a) 0, b) 30, c) 60, d) 90.

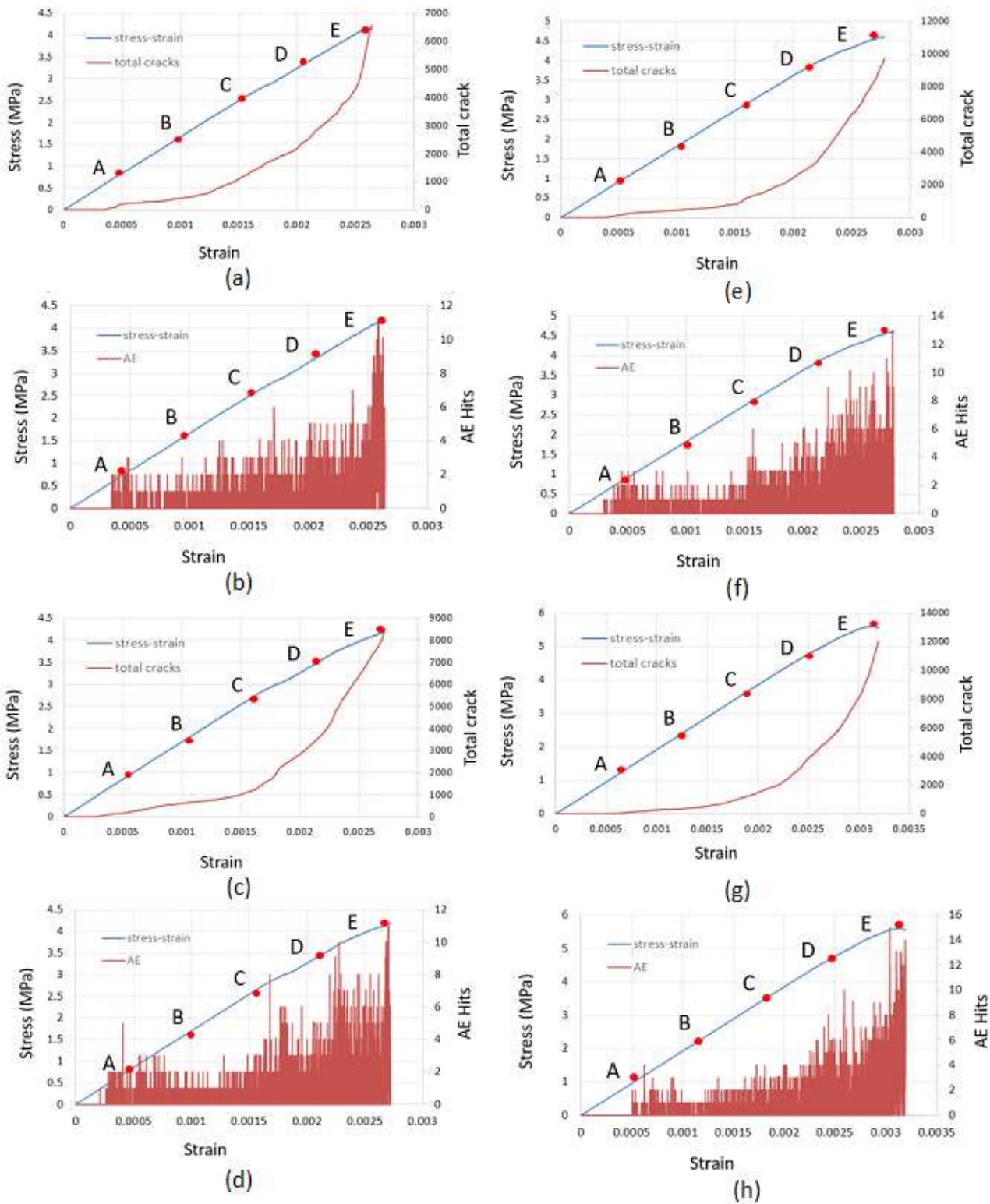


Figure 21

Stress and AE behavior in the test simulation for joint spacing of 3m, a) stress-strain curve and cumulative crack number for joint angle of 0, b) the number of AE hits along the strain curve for joint angle of 0, c) stress-strain curve and cumulative crack number for joint angle of 30, d) the number of AE hits along the strain curve for joint angle of 30, e) stress-strain curve and cumulative crack number for joint angle of 60, f) the number of AE hits along the strain curve for joint angle of 60, g) stress-strain

curve and cumulative crack number for joint angle of 90, h) the number of AE hits along the strain curve for joint angle of 90.

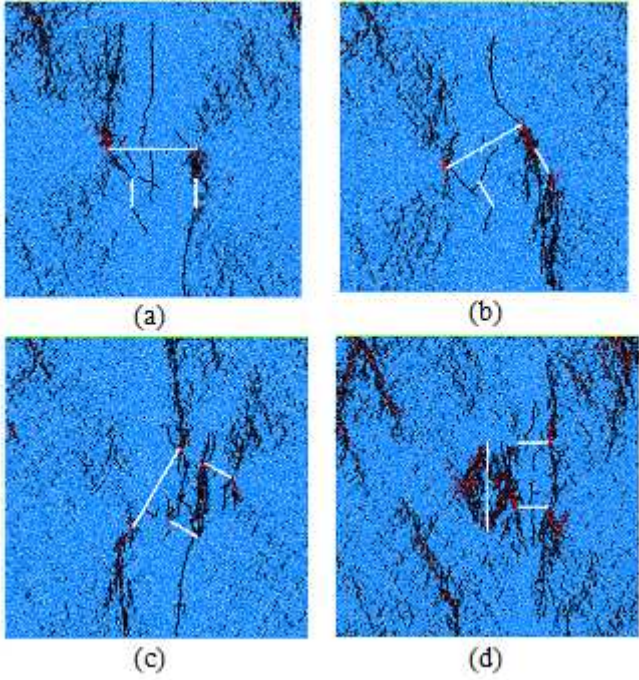


Figure 22

Crack pattern in specimen containing F shape non persistent joints with large joint angle of; a) 0, b) 30, c) 60, d) 90; vertical distance between small joint was 4cm.

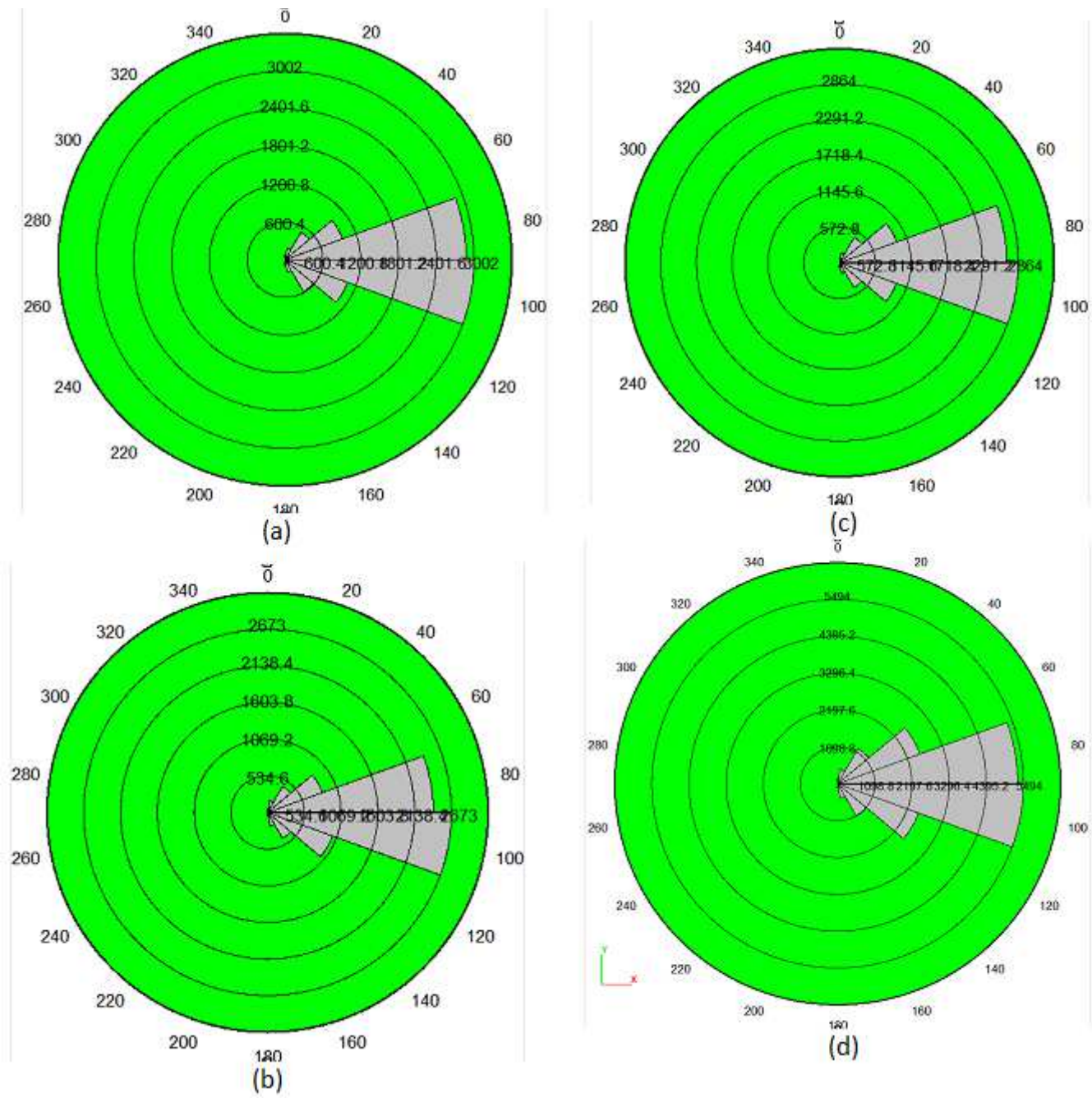


Figure 23

Ross diagram of crack growth for F shape joint with angle of ϕ ; a) 0, b) 30, c) 60, d) 90.

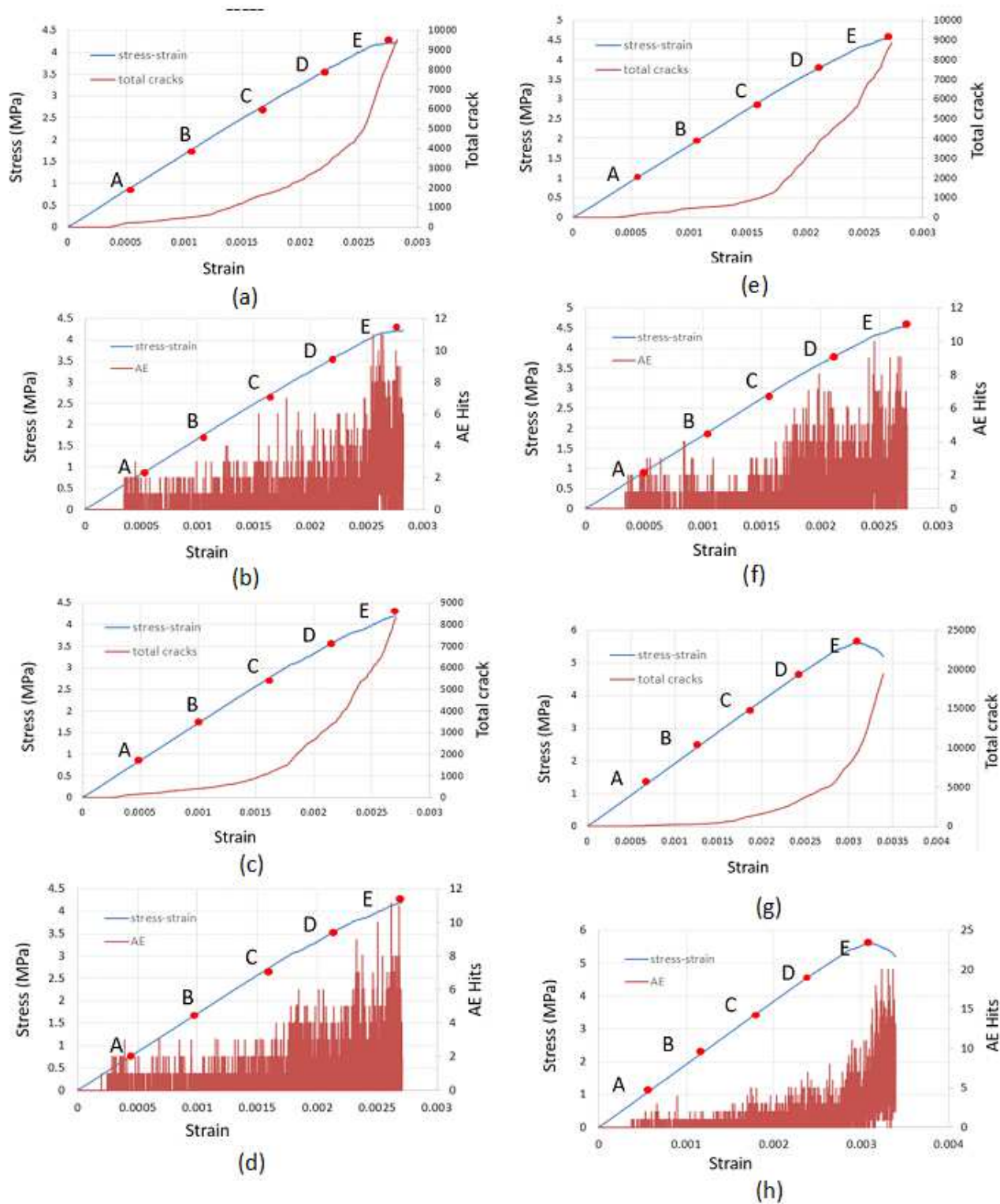


Figure 24

Stress and AE behavior in the test simulation for joint length of 6cm, a) stress-strain curve and cumulative crack number for joint angle of 0, b) the number of AE hits along the strain curve for joint angle of 0, c) stress-strain curve and cumulative crack number for joint angle of 30, d) the number of AE hits along the strain curve for joint angle of 30, e) stress-strain curve and cumulative crack number for joint angle of 60, f) the number of AE hits along the strain curve for joint angle of 60, g) stress-strain

curve and cumulative crack number for joint angle of 90, h) the number of AE hits along the strain curve for joint angle of 90.

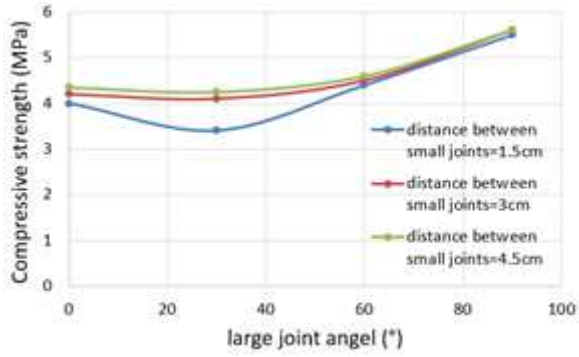


Figure 25

the influence of joint angle on the strength of models.